KRONOS FUSION ENERGY

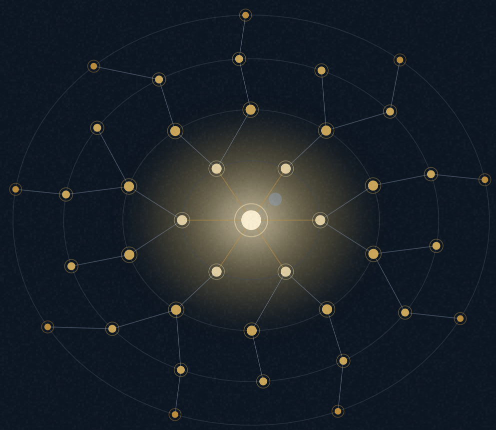

PAPER 2.103 · THE KRONOS 2026 SERIES

Heating and Current-Drive Actuator Systems for a Compact Spherical-Tokamak Breeder: An NBI/ECH/ICRF/LHCD Mix Optimized for Solenoid-Free Sustainment

The heating and current-drive (H&CD) system is what holds a compact breeder's operating point in place, and in a solenoid-poor spherical tokamak (ST) it must sustain almost the...

Read it live — 3-D model · physics validator · film series

BY P I FORD AND G L KULCINSKI

2026 · EDITORIAL EDITION

THE OFFICIAL RECORD

What this document is, and how to read its numbers

This is a combined editorial. It gathers, in one volume, the two design studies Kronos Fusion Energy released in 2026 — a compact spherical-tokamak tritium/helium-3 breeder and a deuterium–helium-3 tandem-mirror generator — together with the intellectual-property estate, the people, and, in the internal edition, the full commercial case. The scientific text is the same text that appears in the arXiv preprints and the journal submissions; the editorial adds the apparatus a reader needs to hold the whole program at once, and nothing in the physics is altered to fit it.

THE HONESTY STANCE IS THE ASSET

Every headline quantity carries an **evidence class** — DERIVED RECOMPUTED MEASURED REQUIREMENT — and, where a number is a modelled extrapolation rather than a demonstrated value, it is labelled as such and its downside is shown next to it. Several quantities in the underlying corpus moved after first publication; where a value has been withdrawn or restated, the record says so plainly. This is deliberate: a diligence team will find the load-bearing assumptions, so the document surfaces them first.

TWO EDITIONS

This volume is issued in two editions. The **public edition** (light) carries the physics and the design only — no dollar, price, or per-kilogram figure appears anywhere in it. The **internal edition** (dark) adds the economics, the funding architecture, and the defense-commercial analysis, and is marked *Confidential* accordingly; it is not for public distribution. Where the commercial case rests on a modelled assumption rather than a demonstrated one, it is labelled as such and its downside is shown alongside it, on the same terms as the physics.

TITLE	The Kronos Fleet — Hyperion · Aegis · MetroVolt: A Combined Design & Commercialization Study
AUTHOR	Priyanca Ford, Founder & CEO, on behalf of Kronos Fusion Energy
EDITION	2026 Combined Editorial · first issue
COMPANION WORKS	The five-paper arXiv drop — (1) Breeder, (2) Burner, (3) REBCO magnet & tape, (4) Direct Energy Conversion, (5) AI/ML/Quantum control — with matching numbered Zenodo deposits, plus the IOP journal and IAEA-FEC submissions. Patents were filed before the drop.
NAMING	Hyperion = the breeder; Aegis (defense) and MetroVolt (data-center) = one generator in two housings. Internal mode letters (D1, L) do not appear on public surfaces.
STATUS	Conceptual design & simulation study. Nothing herein is a construction commitment.

HOW TO READ THIS VOLUME

The fleet at a glance, and the way its numbers are marked

This volume opens with *Orientation*, presents the five research papers as a bound sequence, and closes with the *Apparatus*. *Foundations* sets out the three general results both machines rest on. *Paper One* is the Hyperion breeder; *Paper Two* the Aegis / MetroVolt generator; *Papers Three, Four and Five* are the enabling science — high-field REBCO magnets and tape, direct energy conversion, and the AI / ML / quantum control stack. A *Digital Twin & 3-D Model* part follows, then the *Environmental* profile. The *Economics* and levelized cost and the *Business Case* and diligence record appear in the internal edition only; the *Simulations* proof record and the Apparatus — patent portfolio, team, limitations, and sources — close both editions.

THE FLEET AT A GLANCE

	HYPERION	AEGIS	METROVOLT
Role	Strategic-isotope foundry	Defense installation power	Campus power
Machine	**Spherical tokamak**	**Tandem mirror**	**Tandem mirror**
Fuel	Deuterium–tritium	Deuterium–helium-3	Deuterium–helium-3
Delivers	Tritium · ^{3}He · 14 MeV n	Resilient installation power	Firm campus power
Physics bar	**Fusion gain only**	Closure (gates named)	Closure + lunar ^{3}He
In the fleet	Breeds the fuel	Proves the generator	Commercial destination

HOW THE NUMBERS ARE MARKED

Every headline quantity carries an evidence class — DERIVED from first principles, RECOMPUTED from raw data, MEASURED in hardware, or a REQUIREMENT yet to be met. Financial figures carry a case label and are confined to the internal (confidential) edition. Values that moved after first publication are shown as withdrawn or restated rather than quietly changed. A capability you can evaluate is one whose limits are on the page.

ABSTRACT

Heating and Current-Drive Actuator Systems for a Compact Spherical-Tokamak Breeder: An NBI/ECH/ICRF/LHCD Mix Optimized for Solenoid-Free Sustainment

The heating and current-drive (H&CD) system is what holds a compact breeder's operating point in place, and in a solenoid-poor spherical tokamak (ST) it must sustain almost the entire plasma current non-inductively. We derive and specify that system for the Hyperion breeder from first principles and from frozen, independently reproduced design results. The duty is fixed by the design point: sustain $I_p = 9.66\,MA$ at $R_0 = 1.20\,m$, $B_0 = 8\,T$, $\kappa = 2.0$ in a negative-triangularity ($\delta = -0.30$) regime with $Q = 3.076$ and $P_{\mathrm{fus}} = 85.04\,MW$. A first-principles neoclassical drift-kinetic calculation fixes the self-driven bootstrap fraction at $\mathbf{f_{bs} = 0.155}$, so $I_{\mathrm{CD}} = (1 - f_{\mathrm{bs}})I_p = 8.16\,MA$ must be driven externally; at a normalized current-drive efficiency $\gamma_{\mathrm{CD}} = n_{e20}R_0 I_{\mathrm{CD}}/P_{\mathrm{CD}} = 0.331$ this requires an injected drive power of $P_{\mathrm{CD}} = 118.5\,MW$, dwarfing the gain-basis auxiliary heating power $P_{\mathrm{aux}} = P_{\mathrm{fus}}/Q \approx 27.6\,MW$. The breeder is therefore a current-drive-dominated, deliberately subcritical neutron source (wall-plug $\approx 5.2\,P_{\mathrm{fus}}$), and drive *efficiency*, not raw power, is the quantity to optimise. We write the governing physics as explicit equations — the non-inductive current balance, the Sauter neoclassical bootstrap, the Fisch current-drive efficiency, negative-ion beam stopping and shine-through, the electron-cyclotron dispersion and cutoffs (fundamental $f_{ce} = 224$ Hertzat8 T,\omega_pe/\omega_ce=0.80 , $edge - overdenseelectron - Bernsteinconversion), lower - hybridaccessibility, andtheimpurity - radiationbudget($0.19 MW $perppmoftungsten) - - - andcasttheallocationofpoweracrossthefourtechnologiesasaconstrainednonlinearprogramwhoseKarush - -Kuhn - -Tuckermultipliersmakedriveefficiencythebindingshadowprice. Wegivethecouplednumericalformulation(equilibrium transportbootstrap$ ray/Fokker–Planck fixed-point iteration), the GPU-accelerated code stack that produced every number, and six real-time controllers, each with an explicit acceptance test and admitted to authority only through a maturity gate. The result is an H&CD architecture defined by the physics it must serve, quantitatively benchmarked against the published NBCD/ECCD/LHCD literature, and staged cleanly toward hardware.

Open-access deposit (code & data, CC BY 4.0): DOI 10.5281/zenodo.22645872 · Zenodo community *kronos_fusion_energy*. Explore it live: interactive 3-D model · physics validator.

Keywords: neutral-beam injection · electron-cyclotron current drive · lower-hybrid current drive · bootstrap fraction · solenoid-free sustainment · actuator control · spherical-tokamak breeder

CONTENTS

Table of Contents

NOMENCLATURE

Symbols, units, and the names of things

Q	plasma (fusion) gain, P_{fus}/P_{aux}
Q_E	engineering gain, net electric out / recirculating in
H_{98}	confinement enhancement over the IPB98(y,2) scaling
Z_{eff}	effective ion charge
c_{ee}	electron–electron bremsstrahlung leading coefficient, 2.120022 (exact)
τ_E	energy confinement time
I_p	plasma current
R_0, a	major radius, minor radius
κ, δ	elongation, triangularity
β_N	normalized plasma beta (Troyon-normalized)
TBR	tritium breeding ratio
DEC	direct energy conversion
CF	plant capacity factor (availability)
FOAK / NOAK / BOAK	first / n^{th} / best of a kind
Hyperion	the ST breeder (internal: Mode D2)
Aegis	the generator, defense/installation housing (internal: Mode M)
MetroVolt	the generator, data-center housing (Mode M)

§ 1

Introduction

CURRENT SUSTAINMENT IS THE CENTRAL PROBLEM OF A COMPACT ST BREEDER

A spherical tokamak confines a large plasma current in a small volume, which is what makes it an attractive neutron source and tritium-breeder platform [1,2,3] and, at the same time, what makes its heating and current-drive (H&CD) system the pacing subsystem. The Hyperion breeder holds $I_p = 9.66\,MA$ at a major radius of only $R_0 = 1.20\,m$ behind a centrepost magnet at a peak field of $16.84\,T$, in a negative-triangularity ($\delta = -0.30$) regime chosen because it accesses good confinement without the edge pressure pedestal and the edge-localised-mode (ELM) cycle of conventional H-mode [4,5]. Two features of that design point make current drive, not heating, the dominant duty: the compact machine′s central-solenoid volt-second budget is too small to sustain an inductive flat-top, so the current must be non-inductive; and the self-driven bootstrap fraction is modest — a first-principles neoclassical calculation gives $f_{\rm bs} = 0.155$ — so roughly 85% of a nine-megaampere current must be driven by external actuators for the life of the pulse. The H&CD system is therefore not an auxiliary but the mechanism by which the breeder exists as a steady device.

PHYSICS AND PRIOR ART IN HEATING AND CURRENT DRIVE

The theory of non-inductive current drive is mature. Fisch established the general framework for driving current by selectively increasing the collisionality of resonant electrons [6,7]; Ohkawa and Start, Cordey and Jones developed the theory of beam-driven current with the trapped-electron shielding correction [8,9]; Prater and co-workers reduced electron-cyclotron current drive (ECCD) to a quantitatively benchmarked tool [12,13]; Bonoli reviewed the modern status of lower-hybrid current drive (LHCD) at reactor-relevant parameters [14]; and the fast-wave and minority ion-cyclotron (ICRF) schemes trace to Stix and are now computed with self-consistent full-wave and Fokker–Planck codes [15,16,17]. The self-driven bootstrap current, which sets how much the actuators must supply, is given by the neoclassical formulas of Sauter, Angioni and Lin-Liu and by the drift-kinetic solver NEO [10,11]. The integrated picture — how these sources combine to sustain a steady, profile-controlled equilibrium — is codified in the ITER Physics Basis chapters on auxiliary heating and on steady-state operation [19,20] and is now advanced by real-time, physics-model-based profile control [28,27] and by learned controllers that command actuators directly from measurements [29].

THE GAP AND OUR CONTRIBUTION

What the literature treats as separate objects — a bootstrap calculation [10], a beam-deposition code [21], an ECCD benchmark [13], an LHCD accessibility analysis [14], a learned controller [29] — must, for a compact nuclear ST, be assembled into a single actuator architecture that derives its duty from the frozen design point, writes each source as an explicit governing equation, allocates power by a transparent optimisation whose shadow prices identify the binding quantity, is produced by a reproducible GPU code stack, and is operated by real-time controllers each carrying a pre-registered acceptance test and a graded authority gate. This paper contributes exactly that: the actuator duty as a formal problem (§2); the governing equations of the four sources and the impurity constraint (§3); the actuator-mix allocation as a constrained nonlinear program with its Karush–Kuhn–Tucker (KKT) conditions (§4); the coupled numerical formulation and GPU HPC campaign behind every number (§5); the four-technology complement (§6) and six controllers (§7); the results (§8); a benchmark against the literature (§9); and one honest limitation (§10). Every quantitative claim traces to a frozen result in the Kronos Physics De-Risking Register [39]; serial identifiers (e.g. BR-L2-A6, BOM-07) are given inline so each number is auditable.

§ 2

The actuator duty as a formal problem

The H&CD duty is not a free choice; it is dictated by the design point (table 1). Let the plasma current I_p, fusion power P_{fus}, and gain Q be the frozen anchors, reproduced independently by the zero-dimensional balance (BR-L1-A1) and the negative-triangularity re-anchor audit (BR-L1-A7). Three quantities follow.

Auxiliary heating power (gain basis). By the definition of gain, the auxiliary heating power that sustains the temperature at the operating point is

$$P_{\text{aux}} = \frac{P_{\text{fus}}}{Q} = \frac{85.04\,\text{MW}}{3.076} = 27.6\,\text{MW}.$$

Externally driven current. With a self-driven bootstrap fraction f_{bs}, the non-inductive current balance in the solenoid-free steady state (derived in §3.1) requires the actuators to supply

$$I_{\text{CD}} = (1 - f_{\text{bs}})\, I_p = (1 - 0.155) \times 9.66\,\text{MA} = 8.16\,\text{MA},$$

using the neoclassical value $f_{\text{bs}} = 0.155$ (BR-L2-A6, BR-L2-A16).

Injected drive power. At the normalized current-drive efficiency of the beam-driven design solution (BOM-07), $\gamma_{\text{CD}} = n_{e20} R_0 I_{\text{CD}} / P_{\text{CD}} = 0.331$ (inside the 0.20–0.40 physical band), the injected power required to drive I_{CD} is

$$P_{\text{CD}} = \frac{n_{e20}\, R_0\, I_{\text{CD}}}{\gamma_{\text{CD}}} = \frac{4.00 \times 1.20 \times 8.16}{0.331} = 118.5\,\text{MW},$$

with the line-averaged density $n_{e20} = f_G\, n_{\text{GW}} = 0.30 \times 13.34 = 4.00$ ($10^{20}\,\text{m}^{-3}$) fixed by the Greenwald fraction $f_G = 0.30$ (KX-L1-A2). Equations (1)–(3) expose the defining tension of a breeder: the power needed to *sustain the current*, $P_{\text{CD}} = 118.5\,MW$, is more than four times the power needed to *sustain the gain*, $P_{\text{aux}} \approx 27.6\,MW$. The machine is a deliberately subcritical neutron source, with a wall-plug demand of order $5.2\,P_{\text{fus}}$ (figure 2; BOM-07/09); it is not, and is not presented as, a net-electric device. Because current drive dominates the power balance, current-drive *efficiency* — amperes per watt delivered on the right flux surface — is the single highest-value quantity for the system to optimise. §4 makes this precise as a shadow price.

DUTY QUANTITY	VALUE	BASIS (SERIAL)
plasma current I_p	9.66 MA	design anchor (BR-L1-A1/A7)
fusion power P_{fus}	85.04 MW	design anchor (BR-L1-A1)
gain Q	3.076	design anchor (BR-L1-A1)
gain-basis heating $P_{\text{aux}} = P_{\text{fus}}/Q$	27.6 MW	eq. (1)
bootstrap fraction f_{bs}	0.155	NEO drift-kinetic (BR-L2-A6/A16)
externally driven current I_{CD}	8.16 MA	eq. (2); BOM-07
normalized CD efficiency γ_{CD}	0.331	BOM-07 (band 0.20–0.40)
injected drive power P_{CD}	118.5 MW	eq. (3); BOM-07
deposition regime	off-axis, $\delta = -0.30$	NT profile control (BR-L2-A19)

The heating and current-drive duty implied by the frozen design point. Every entry follows from a design anchor or a first-principles result in the register [39].

The negative-triangularity regime adds a *deposition* requirement. Holding a quiet, subcritical, ELM-free edge at $\delta = -0.30$ (BR-CX-08) depends on where power and current are deposited across the profile, which places a premium on steerable, off-axis actuators rather than fixed central deposition (figure 4). The duty is thus threefold: deliver the heating implied by the gain, drive $8.16\ MA$ as efficiently as possible, and place both on target across the profile. This is the physics context of the negative-triangularity confinement result [doi:10.5281/zenodo.22645722; https://www.kronosfusionenergy.com/publications/negative-triangularity-confinement.html]companionNT and of the current-drive and bootstrap companion study [doi:10.5281/zenodo.22645758; https://www.kronosfusionenergy.com/publications/current-drive-and-bootstrap.html]companionCD.

§ 3

Governing equations of the four sources

NON-INDUCTIVE CURRENT BALANCE

The toroidal plasma current evolves under the circuit equation coupling it to the poloidal-flux Ψ [19,20],

$$L_p \frac{\mathrm{d}I_p}{\mathrm{d}t} = V_{\mathrm{ext}} - R_p\big(I_p - I_{\mathrm{bs}} - I_{\mathrm{CD}}\big),$$

with plasma inductance L_p, resistance R_p, external (solenoid) loop voltage V_{ext}, and the self-consistent bootstrap and driven currents $I_{\mathrm{bs}}, I_{\mathrm{CD}}$. Integrating over a flux surface, the surface-averaged Ohm's law reads

$$\langle E\cdot B\rangle = \eta_{\mathrm{nc}}\Big(\langle j_{\parallel}B\rangle - \langle j_{\mathrm{bs}}\cdot B\rangle - \langle j_{\mathrm{CD}}B\rangle\Big),$$

where η_{nc} is the neoclassical parallel resistivity [10]. In a solenoid-free steady state the volt-second source is exhausted, $V_{\mathrm{ext}} \to 0$ and $\langle E\cdot B\rangle \to 0$, so $\mathrm{d}I_p/\mathrm{d}t = 0$ forces every ampere to be non-inductive:

$$I_p = I_{\mathrm{bs}} + I_{\mathrm{CD}}, \qquad I_{\mathrm{bs}} = f_{\mathrm{bs}} I_p, \qquad I_{\mathrm{CD}} = (1 - f_{\mathrm{bs}}) I_p.$$

Equation (6) is the current budget of figure 2: a $1.50\,MA$ bootstrap seed and a $8.16\,MA$ externally driven remainder. The solenoid-free flat-top it defines is the operating point of the startup and ramp companion study [doi:10.5281/zenodo.22645760; https://www.kronosfusionenergy.com/publications/solenoid-free-startup.html]companionSF; the reduced volt-second model puts the current-drive-limited ramp at $\sim 43\,s$ with $\Psi_p \approx 20\,weber$ (BR-CX-07).

NEOCLASSICAL BOOTSTRAP CURRENT

The self-driven current follows from the neoclassical parallel force balance. In the Sauter form [10],

$$\langle j_{\mathrm{bs}}\cdot B\rangle = -I(\psi)\, p_e \left[\mathcal{L}_{31}\frac{p}{p_e}\frac{\partial \ln p}{\partial\psi} + \mathcal{L}_{32}\frac{\partial \ln T_e}{\partial\psi} + \mathcal{L}_{34}\,\alpha\,\frac{p_i}{p_e}\frac{\partial \ln T_i}{\partial\psi}\right],$$

where $I(\psi) = RB_\phi$, $p = p_e + p_i$, and the transport coefficients $\mathcal{L}_{31}, \mathcal{L}_{32}, \mathcal{L}_{34}$ and the ion term α are rational functions of the effective trapped-particle fraction

$$f_t = 1 - \frac{(1-\varepsilon)^2}{\sqrt{1-\varepsilon^2}\,(1 + 1.46\sqrt{\varepsilon})}, \qquad \varepsilon = \frac{a}{R_0} = 0.40,$$

and of collisionality ν_{*e}. The large inverse aspect ratio of an ST gives a high trapped fraction ($f_t \approx 0.63$ at $\varepsilon = 0.40$), which enhances the bootstrap coefficients; the modest *value* $f_{\mathrm{bs}} = 0.155$ nonetheless results because the pressure and density profiles at the negative-triangularity operating point are relatively flat and $q_{95} = 3.0$ is low. Rather than rely on the analytic coefficients of equation (7), the frozen value is taken from a first-principles solution of the drift-kinetic equation by NEO [11] (BR-L2-A6): $f_{\mathrm{bs}} = 0.15501$, cross-checked against the Sauter parallel bootstrap in identical normalisation (BR-L2-A16). This is the number that enters equations (2) and (6).

CURRENT-DRIVE EFFICIENCY

For any wave- or beam-driven scheme, the driven current density relates to the absorbed power density p_d through the Fisch efficiency [6],

$$\frac{j_{\mathrm{CD}}}{p_d} = \frac{e}{m_e\,\nu_{\mathrm{th}}\,v_{\mathrm{th}}}\;\frac{\hat{s}\cdot\nabla_u \chi}{\hat{s}\cdot\nabla_u\big(\tfrac{1}{2}u^2\big)},$$

where $\chi(u)$ is the adjoint (Spitzer–Härm) response function, $u = v/v_{\mathrm{th}}$ the normalized velocity, and $\hat{s}$ the direction of momentum input in velocity space. Integrating over the plasma and non-dimensionalising gives the engineering figure of merit used throughout this paper,

$$\gamma_{\mathrm{CD}} \equiv \frac{n_{e20}\,R_0\,I_{\mathrm{CD}}}{P_{\mathrm{CD}}} \quad \big[10^{20}\,\mathrm{A\,W^{-1}\,m^{-2}}\big],$$

whose numerical value 0.331 at the design point (BOM-07) sits inside the $0.20–0.40$ band typical of negative-ion NBCD in a device of this size and density. Equation (10) is the axis of figure 3: the injected power scales inversely with $\gamma_{\rm CD}$, so a 20% improvement in drive efficiency buys a $\sim 24\,MW$ reduction in $P_{\rm CD}$ at fixed $I_{\rm CD}$ — the payoff that motivates the current-drive-efficiency controller of §7.

NEUTRAL-BEAM DEPOSITION, DRIVEN CURRENT AND SHINE-THROUGH

The workhorse actuator is negative-ion neutral-beam injection. A neutral of energy E_b deposits by charge-exchange and impact ionisation with a mean free path $\lambda_b(E_b) = [n_e\sigma_{\rm stop}(E_b)]^{-1}$; integrating the attenuation along the chord ℓ gives the surviving (shine-through) fraction

$$S = \exp\!\left(-\int_0^L n_e(\ell)\,\sigma_{\rm stop}(E_b)\,{\rm d}\ell\right),$$

which must be held below the far-wall power-load limit by the shine-through monitor (§7). The choice of $E_b = 1\,MeV$ D$^-$ (BOM-07) is forced by two facts: positive-ion neutralisation efficiency collapses above $\sim 100\,keV$, mandating negative ions at this energy; and at $n_{e20} = 4.0$ over a chord of order $2a \approx 0.96\,m$ a lower energy would deposit too shallowly and raise S. The beam-driven current carries the trapped-electron shielding correction of Ohkawa and Start–Cordey [8,9],

$$I_{\rm NB} = I_f\left[1 - \frac{Z_b}{Z_{\rm eff}}\big(1 - G(Z_{\rm eff},\varepsilon)\big)\right], \qquad G(Z_{\rm eff},\varepsilon) = \left[1.55 + \tfrac{0.85}{Z_{\rm eff}}\right]\sqrt{\varepsilon} - \left[0.20 + \tfrac{1.55}{Z_{\rm eff}}\right]\varepsilon,$$

with I_f the fast-ion current and G the trapped-electron back-current factor; the deposition profile $j_{\rm NB}(r)$ is computed by the Monte-Carlo fast-ion module NUBEAM [21]. In the ST the large ε makes G sizeable, partially recovering the electron shielding and improving NBCD efficiency relative to a conventional tokamak. Reconciling equation (12) with the design current gives the $118.5\,MW$, eight-beamline ($N{+}1$ redundant), $1\,MeV$ D$^-$ solution of BOM-07.

ELECTRON-CYCLOTRON WAVES: DISPERSION, CUTOFFS AND BERNSTEIN CONVERSION

Electron-cyclotron heating and current drive (ECH/ECCD) deposit power at the cyclotron resonance $\omega = n\,\omega_{ce}$, $\omega_{ce} = eB/m_e$, giving a fundamental $f_{ce} = 28$ Hertz× B_0=224 at $B_0 = 8\,T$ (BOM-08; figure 4). Wave access is governed by the cold-plasma cutoffs. The ordinary (O-)mode is cut off at the plasma frequency $f_{pe} = 8.98\sqrt{n_e[{\rm cm}^{-3}]}$ Hz $= 180$ Hertz*for* n_e20=4.0$; the extraordinary (X-)mode right-hand cutoff is

$$\omega_R = \tfrac{1}{2}\left(\omega_{ce} + \sqrt{\omega_{ce}^2 + 4\omega_{pe}^2}\right).$$

The controlling ratio is $\omega_{pe}/\omega_{ce} = 180/224 = 0.80$: the core is *underdense*, so conventional O-/X-mode ECH is accessible for central deposition and profile control, but the edge is *overdense* ($\omega_{pe} > \omega_{ce}$), where power must be coupled through electron-Bernstein-wave (EBW) mode conversion [18]. The ECCD efficiency follows the Fisch–Boozer mechanism of selective electron heating supplemented by the Ohkawa trapped-particle current [7,12,13], and its narrow, steerable deposition (figure 4) is set by the resonance location, which the launch mirror moves in real time. A complement of $\sim 15{+}2$ gyrotrons at $1\,MW$ delivers $\sim 15\,MW$; the 224 Hertz$ tube is at the frontier of gyrotron development and is flagged as such (BOM-08).

ION-CYCLOTRON FAST WAVES AND IMPEDANCE MATCHING

Ion-cyclotron heating (ICRF) couples bulk and minority ions through the fast magnetosonic wave, whose cold-plasma perpendicular refractive index is

$$n_\perp^2 = \frac{(R - n_\parallel^2)(L - n_\parallel^2)}{S - n_\parallel^2}, \qquad S = \tfrac{1}{2}(R + L),$$

with Stix parameters R, L, S [15]; minority heating deposits at $\omega = Z_m eB/m_m$ and is computed self-consistently by full-wave plus Fokker–Planck solvers [16,17]. The antenna presents a plasma-dependent loading resistance R_c that varies with edge density and the plasma–antenna gap, so the coupled power is throttled by the reflection coefficient

$$|\Gamma|^2 = \left|\frac{Z_L - Z_0}{Z_L + Z_0}\right|^2,$$

where Z_L is the (time-varying) antenna load impedance and Z_0 the transmission-line impedance. Minimising $|\Gamma|^2$ in real time is the task of the impedance matcher (§7), which must run on a fast loop because Z_L changes faster than the profile-rate controllers above it. The same fast-wave physics, applied in the separate mirror burner as ICRF alpha-channelling, is the subject of the burner RF study (BU-L2-A8) and is distinguished from the breeder duty in §6.1.

LOWER-HYBRID ACCESSIBILITY

Lower-hybrid current drive (LHCD) is the most efficient off-axis actuator per watt but is constrained by wave accessibility: a launched parallel index below the accessibility limit is reflected before it reaches the core,

$$n_{\|,\mathrm{acc}} = \frac{\omega_{pe}}{\omega_{ce}} + \sqrt{1 + \frac{\omega_{pe}^2}{\omega_{ce}^2} - \frac{\omega_{pi}^2}{\omega^2}},$$

and the LHCD efficiency scales as $\gamma_{\mathrm{LH}} \propto n_{\|}^{-2}$ [6,14]. At $\omega_{pe}/\omega_{ce} = 0.80$ the accessibility floor is modest, so LHCD is retained as an efficient outer-radius actuator in the complement, supporting the non-inductive flat-top where the bootstrap seed and NBCD leave a gap (figure 4).

IMPURITY-RADIATION CONSTRAINT

Sustaining $27.6\,MW$ of heating *cleanly* requires keeping wall-sputtered high-Z impurities scarce, because core line radiation scales with the cooling function $L_Z(T_e)$,

$$P_{\mathrm{rad}} = \int n_e \sum_Z n_Z \, L_Z(T_e) \, \mathrm{d}V,$$

and tungsten radiates strongly even at core temperature: a collisional-radiative calculation gives $L_W(15\,keV) = 5.7e - 32\,Wm^3$ against $L_{\mathrm{Ar}} = 1.45e - 33\,Wm^3$ (BR-L2-A29), a factor of 39. The resulting sensitivity is a tungsten tolerance of $0.19\,MW$ of radiated power per part-per-million of core concentration (figure 5). The heating-mix and power controllers therefore schedule against an impurity budget as well as a power target, and the impurity-transport controller (KFE-CF-BR-075) holds core c_W below the limit set by equation (17).

§ 4

Actuator-mix allocation as a constrained optimisation

The complement is functionally redundant — heating and current drive are each served by more than one technology — so the assignment of power $\{P_k\}$ across the actuators $k \in \{\mathrm{NBI}, \mathrm{ECH}, \mathrm{ICRF}, \mathrm{LHCD}\}$ is an optimisation, not a fixed recipe. We pose it as the constrained nonlinear program

$$\begin{aligned} \min_{\{P_k\}} \quad & \sum_k P_k \\ \text{s.t.} \quad & \sum_k I_{\mathrm{CD},k}(P_k) + f_{\mathrm{bs}} I_p = I_p, && \text{(current)} \\ & \sum_k \eta_{h,k} P_k + P_\alpha \geq P_{\mathrm{aux}}, && \text{(heating)} \\ & \left\| \, j_{\mathrm{tot}}(r) - j_{\mathrm{tgt}}(r) \, \right\| \leq \delta_j, && \text{(deposition/profile)} \\ & q''_{\mathrm{wall}} \leq q''_{\mathrm{max}}, \quad S \leq S_{\mathrm{max}}, && \text{(shine-through/wall)} \\ & P_{\mathrm{rad}}(c_{\mathrm{imp}}) \leq P_{\mathrm{rad,max}}, && \text{(impurity)} \\ & 0 \leq P_k \leq P_{k,\mathrm{max}}. && \text{(actuator bounds)} \end{aligned}$$

The Lagrangian is $\mathcal{L} = \sum_k P_k + \lambda_I g_I + \lambda_h g_h + \mu^\top h$ with g_I the current constraint (18); the stationarity (KKT) condition with respect to each actuator power is

$$1 - \lambda_I \frac{\partial I_{\mathrm{CD},k}}{\partial P_k} - \lambda_h \, \eta_{h,k} - \sum_j \mu_j \frac{\partial h_j}{\partial P_k} = 0.$$

When the current constraint (18) is the binding one — the situation of a current-drive-dominated breeder — its multiplier reduces to the marginal power per marginal ampere,

$$\lambda_I = \left(\partial I_{\mathrm{CD},k} / \partial P_k \right)^{-1} \propto \gamma_{\mathrm{CD}}^{-1},$$

i.e. the *shadow price of current is the inverse of drive efficiency*. Equation (20) is the formal statement of the paper's central claim: because I_{CD} is the binding constraint and λ_I scales as $1/\gamma_{\mathrm{CD}}$, every marginal improvement in current-drive efficiency relaxes the whole program, which is why the mix optimiser assigns the current burden to the highest-γ_{CD} actuator subject to the deposition and wall constraints, and why the efficiency optimiser is the highest-value controller in the stack. The optimum is computed offline by sequential quadratic programming and tracked online by a linearised quadratic program (§7).

§ 5

Computational methodology: the GPU HPC campaign

COUPLED FIXED-POINT FORMULATION

The source terms of §3 are not independent: the bootstrap depends on the pressure profile, which depends on where heating is deposited; the driven current depends on the equilibrium, which depends on the total current profile. The self-consistent operating point is therefore the fixed point of the coupled map

$$\big(\psi,\, T_{e,i},\, n_e,\, j_{\rm bs},\, j_{\rm CD}\big)^{(m+1)} = \mathcal{F}\big[\big(\psi,\, T_{e,i},\, n_e,\, j_{\rm bs},\, j_{\rm CD}\big)^{(m)}\big],$$

where $\mathcal{F}$ chains the free-boundary equilibrium solver (FreeGS/FreeGSNKE [26], BR-L1-A12/BR-L2-A19), the flux-driven transport solver (TGYRO with TGLF/CGYRO fluxes [24,25], BR-L1-A11/BR-L2-A17), the neoclassical bootstrap solver (NEO [11], BR-L2-A6), and the ray-tracing plus bounce-averaged Fokker–Planck current-drive solver (GENRAY+CQL3D [23,22] and NUBEAM [21] for the beams). The iteration is advanced by Picard update with under-relaxation,

$$x^{(m+1)} = (1-\omega_r) \qquad x^{(m)} + \omega_r\,\mathcal{F}[\qquad x^{(m)}], \qquad \omega_r \in (0,1],$$

and is declared converged when the maximum relative change across all fields falls below tolerance,

$$\max_i \frac{\|x_i^{(m+1)} - x_i^{(m)}\|_2}{\|x_i^{(m+1)}\|_2} < 10^{-3}.$$

Under-relaxation ($\omega_r \approx 0.5$) is required near the negative-triangularity marginal state, where the transport solver exhibits stiff limit-cycle behaviour (TGYRO residual 0.61 noted at BR-L1-A11).

DISCRETISATION OF THE KINETIC OPERATORS

Two of the solvers carry the physics that sets the frozen numbers, and their discretisations bound the accuracy of $f_{\rm bs}$ and $\gamma_{\rm CD}$. NEO expands the drift-kinetic distribution in a spectral basis — Legendre polynomials in pitch angle ξ and energy polynomials in v — and solves the resulting linear system for the neoclassical flows; $f_{\rm bs}$ is converged in the spectral resolution (n_ξ, n_v) to the reported 0.15501. CQL3D solves the bounce-averaged Fokker–Planck equation on a two-dimensional (v,ξ) velocity grid,

$$\frac{\partial f}{\partial t} = \mathcal{C}[f] + \mathcal{Q}_{\rm rf}[f] + \mathcal{S}_{\rm nb},$$

with $\mathcal{C}$ the Coulomb collision operator, $\mathcal{Q}_{\rm rf}$ the quasilinear diffusion supplied by the GENRAY ray spectrum, and $\mathcal{S}_{\rm nb}$ the beam source; the collision operator is differenced by the Chang–Cooper scheme to preserve positivity and the Maxwellian null space, and the driven current is the parallel moment $j_{\rm CD} = e\int v_\parallel f\, {\rm d}^3v$. The burner RF companion (BU-L2-A8) uses the reduced two-dimensional form of equation (24) for ICRF alpha-channelling.

GPU ACCELERATION, PROBLEM SCALE AND REPRODUCIBILITY

Every quantitative result in this paper was produced by the NVIDIA GPU HPC campaign on the Kronos Lambda fleet (A100/H100/A10 accelerators), with the fastest reduced-order and analytic reconciliation steps run on the in-house HPC node. The GPU-resident workloads are the gyrokinetic and quasilinear transport solves (CGYRO and TGLF, whose spectral operators map onto the accelerator), the NEO drift-kinetic linear solve, and the Monte-Carlo transport used for beam-port streaming and shine-through wall loading: the neutronics balance that fixes the shield and streaming penalty was run with OpenMC/ENDF-B-VIII.0 at 1.2×10^8 histories (BR-L1-A5), and the port-area and streaming study (BOM-06) resolves the -0.4% tritium-breeding-ratio penalty of the beam dog-leg (figure 5). The $\gamma_{\rm CD}$ sensitivity band of figure 3 and the global uncertainty ranking were swept with a 4×10^4-sample Monte-Carlo (KX-L1-A5). Reproducibility is enforced at the level of frozen anchors: the campaign independently reproduces $Q = 3.076$, $P_{\rm fus} = 85.04\,MW$, $I_p = 9.66\,MA$ (BR-L1-A1), $f_{\rm bs} = 0.155$ (BR-L2-A6) and the current-drive solution $I_{\rm CD} = 8.16\,MA$, $P_{\rm CD} = 118.5\,MW$ (BOM-07), each tagged by its serial. The verification-first methodology and byte-for-byte provenance for the whole stack are documented in the verification companion [doi:10.5281/zenodo.22645710; https://www.kronosfusionenergy.com/publications/verification-and-validation-47-code-provenance.html]companionVV and the code-by-code backbone [doi:10.5281/zenodo.22645866; https://www.kronosfusionenergy.com/publications/the-code-by-code-verification-backbone-role-version-and.html]companionCB. No cost, budget, or compute-spend figure is reported anywhere in this work.

§ 6

The actuator complement

Four heating and current-drive technologies cover the duty, each with a distinct role (figure 1, table 2):

NBI — the workhorse for off-axis heating and current drive (eqs. 12,11): $118.5\ MW$ across eight $1\ MeV$ D$^-$ beamlines ($N{+}1$ redundant), 67% of the port-area budget (BOM-06/07).
ECH/ECCD — steerable, localised deposition for profile control, set by a movable launch mirror; $\sim 15{+}2$ gyrotrons at 224 Hertz*deliver* \sim15 MW$, with EBW conversion for the overdense edge (BOM-08).
ICRF — bulk/minority ion heating through the fast wave (eqs. 14,15), impedance-matched in real time.
LHCD — efficient outer-radius current drive within the accessibility limit (eq. 16), supporting the non-inductive flat-top. itemize
The complement is deliberately redundant in function, which is what makes the mix optimisation of §4 meaningful: the optimiser can trade among technologies to meet a target at least power or to place deposition where profile control demands.

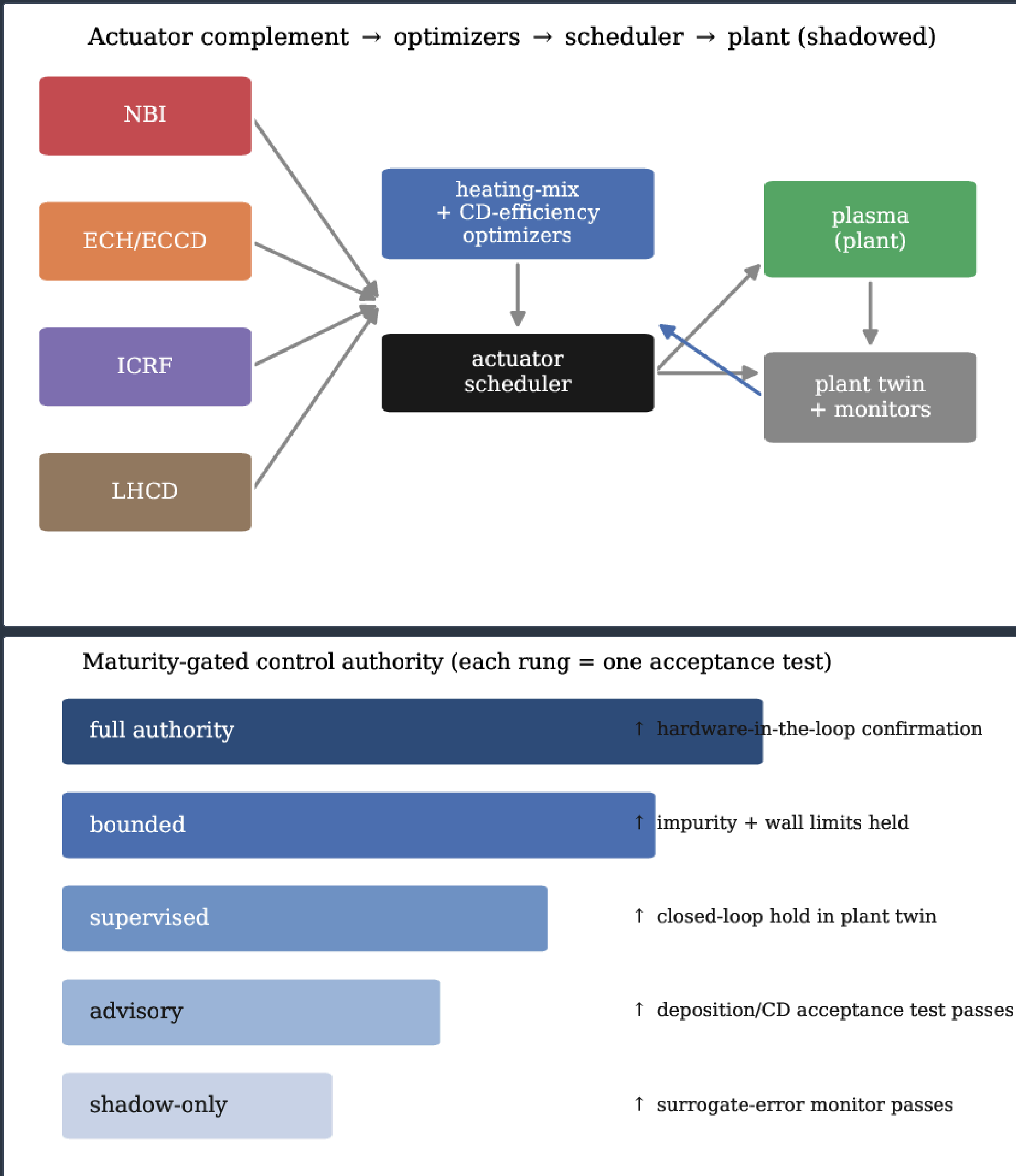

(Schematic.) The actuator complement and its real-time control. Four technologies (left) deliver power and current; a shadowing plant twin and monitors feed the heating-mix and current-drive-efficiency optimisers (§4), which drive the actuator scheduler. Structure only; no data values shown.

ACTUATOR	ROLE	GOVERNING EQN.\	DESIGN FIGURE (SERIAL)
NBI (D^-, 1 MeV)	off-axis heating + CD	(12),(11)	118.5 MW, 8 beamlines (BOM-07)
ECH/ECCD (224 $Hertz)	localised profile control	(13)	$\sim 15\,MW$, 15+2 tubes (BOM-08)
ICRF (fast wave)	bulk/minority ion heating	(14),(15)	antenna-loading matched (BU-L2-A8)
LHCD	efficient outer-radius CD	(16)	within accessibility band

The four-technology actuator complement: role, governing equation, design figure, and register serial.

CONTRAST WITH THE BURNER: TWO DISTINCT MAGNETS, TWO DISTINCT RF DUTIES

The breeder H&CD system described here is specific to the compact ST at a centrepost peak field of $16.84\,T$. The separate Kronos mirror burner is a distinct product with a distinct magnet — a high-field plug coil at $26.49\,T$ — and a distinct RF duty: there, ICRF alpha-channelling and an ECH thermal barrier hold the central electron temperature that sets the direct-energy-conversion spectrum, worth a large multiplier on the burner gain ($Q_E = 1.318$ at $\eta_{\mathrm{DEC}} = 0.49$; AG-CX-05, BU-L2-A8). The two magnets and their heating systems are never conflated — breeder centrepost at $16.84\,T$, burner plug at $26.49\,T$, separate devices with separate complements — and this paper specifies only the breeder's.

§ 7

The six real-time controllers

Six real-time controllers operate the complement (table 3). Each is specified against the duty of §2 and the governing equations of §3, and each is admitted to authority only after it passes an explicit acceptance test in high-fidelity simulation — the maturity-gated pattern the Kronos control architecture applies uniformly (figure 1).

CONTROLLER	FUNCTION	EQN.\	CLASS	ACCEPTANCE TEST (SERIAL)
power controller	NBI/RF/ECH power to set-point	(1)	twin	power tracks set-point (KFE-CF-SH-045)
heating-mix optimiser	allocate among actuators	(18)	twin	target met at least power (KFE-CF-BR-074)
CD-efficiency optimiser	maximise driven A/W	(20)	GPU	drive efficiency improved (KFE-CF-BR-073)
ECH mirror-steering	place ECCD on target	(13)	twin	deposition on target (KFE-CF-BR-072)
NBI shine-through monitor	protect the far wall	(11)	twin	shine-through within limit (KFE-CF-SH-113)
RF impedance matcher	minimise reflected power	(15)	RT	reflected power minimised (KFE-CF-SH-114)

The six heating and current-drive controllers: function, governing equation, real-time class, acceptance test, and register serial. “twin” loops run on the digital-twin node; “GPU” loops on the accelerator tier; “RT” loops on the FPGA-class fast tier.

The controllers form a hierarchy (figure 1). The heating-mix and current-drive-efficiency optimisers (KFE-CF-BR-074/073) decide *what* to run and *how much*, solving the program of §4; beneath them the power controller (KFE-CF-SH-045), ECH mirror-steering (KFE-CF-BR-072) and impedance matcher (KFE-CF-SH-114) execute on the hardware; and the shine-through monitor (KFE-CF-SH-113) caps beam power before the far wall is overloaded. The impedance matcher runs on a fast (FPGA-class) loop because antenna loading changes faster than the twin-rate controllers above it, while the efficiency optimiser runs on the GPU tier because the actuator-space search is compute-intensive. A bootstrap-current estimator (KFE-CF-BR-117) supplies f_{bs} to the optimisers and an impurity-transport controller (KFE-CF-BR-075) enforces the radiation budget of equation (17). This suite composes with the wider real-time control set — profile, shape, vertical-stability, q-profile and solenoid-free-ramp controllers — described in the control-suite companion [doi:10.5281/zenodo.22645809; https://www.kronosfusionenergy.com/publications/a-real-time-control-suite-for-a-compact-negative-triang.html]companionRTC and inherits the plant-shadowing pattern of the four-twin architecture [doi:10.5281/zenodo.22645805; https://www.kronosfusionenergy.com/publications/four-coupled-digital-twins-for-a-compact-spherical-toka.html]companionTwin.

THE SHARED, DEMONSTRATED CONTROL PATTERN

The six controllers are not built from scratch; they instantiate a control pattern already reduced to practice elsewhere in the Kronos architecture — a fast learned surrogate of the plant, a fused multi-sensor estimate, and a controller gated into authority only after clearing an explicit acceptance criterion. The binding of verification credibility to runtime authority is formalised in the maturity-gate companion [doi:10.5281/zenodo.22645795; https://www.kronosfusionenergy.com/publications/maturity-gated-actuation-authority.html]companionMG: a controller that has passed only its surrogate-error monitor may advise but not command, while full authority requires the closed-loop hold plus a hardware-in-the-loop confirmation (figure 1). Each H&CD controller therefore earns authority by holding its target in closed-loop simulation before it acts on hardware, and its development is an instantiation of a proven method on a staged schedule rather than an open research question.

§ 8

Results and verification

THE CURRENT AND POWER BUDGETS

Figure 2 shows the current budget of equation (6): a $1.50\,MA$ bootstrap seed ($f_{\text{bs}} = 0.155$) and a $8.16\,MA$ externally driven remainder, summing to the frozen $9.66\,MA$. Figure 2 shows the power ledger: the $85.04\,MW$ fusion power, the $27.6\,MW$ gain-basis heating, the $118.5\,MW$ injected drive power, and the wall-plug demand of $\approx 439\,MW$ ($5.2\,P_{\text{fus}}$) that makes the breeder subcritical by design. Figure 3 plots the drive-power–efficiency relation of equation (10), with the design duty at $(8.16\,MA, 118.5\,MW)$ on the $\gamma_{\text{CD}} = 0.331$ contour and the 0.20–0.40 band bracketing it; the inverse scaling is the quantitative basis for prioritising drive efficiency.

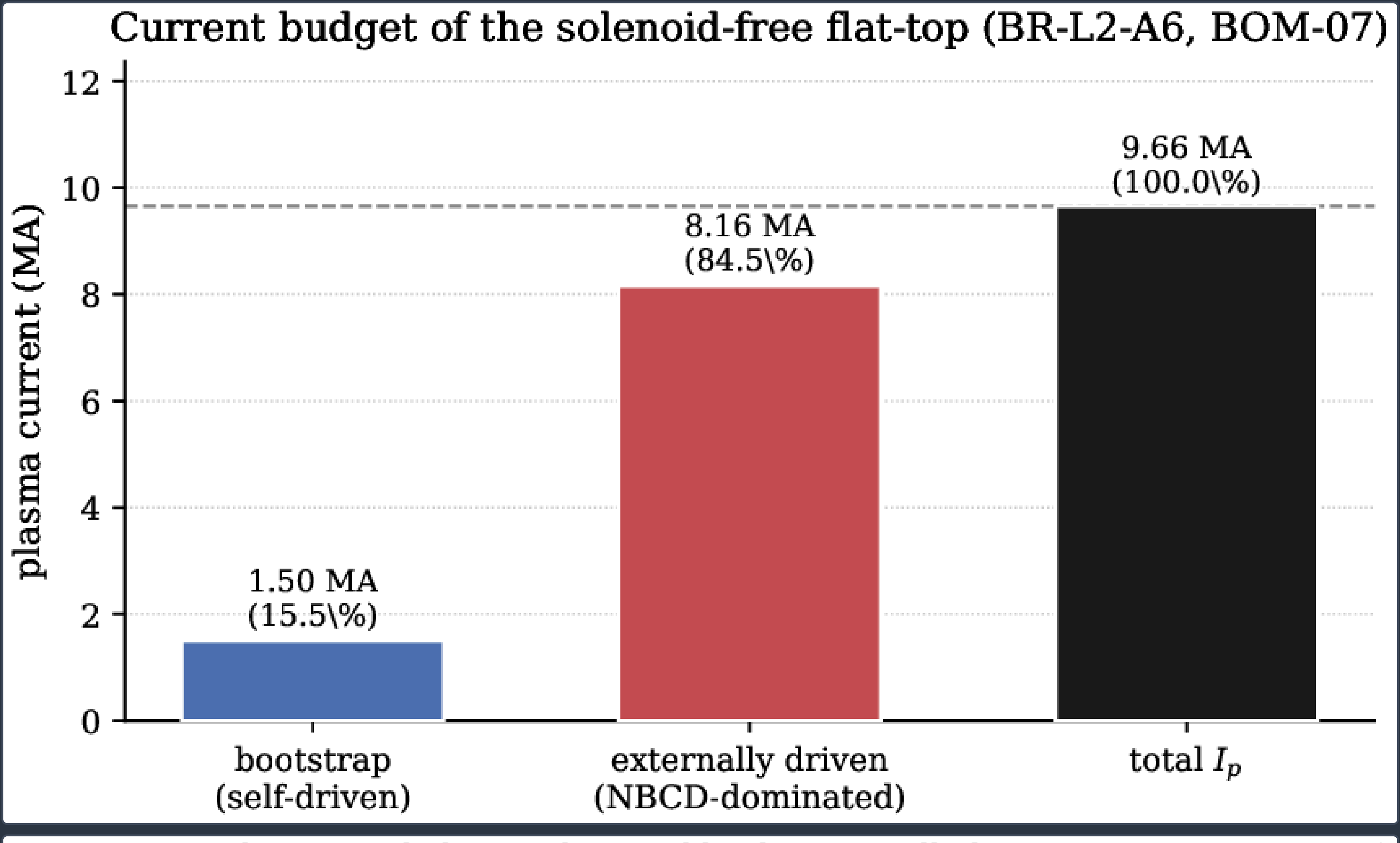

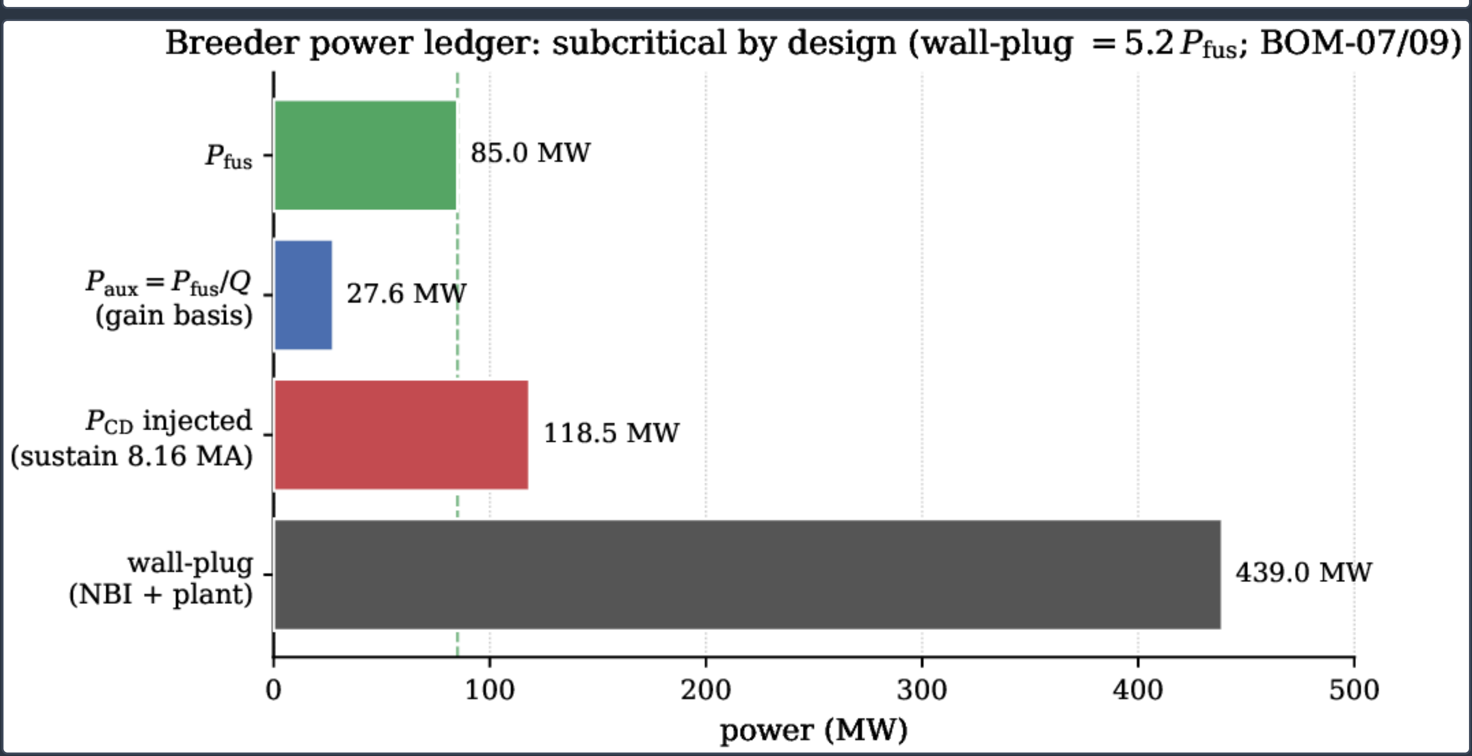

Current budget of the solenoid-free flat-top (eq. 6; BR-L2-A6, BOM-07): a 1.50 MA bootstrap seed and a 8.16 MA externally driven remainder sum to $I_p = 9.66\,MA$.

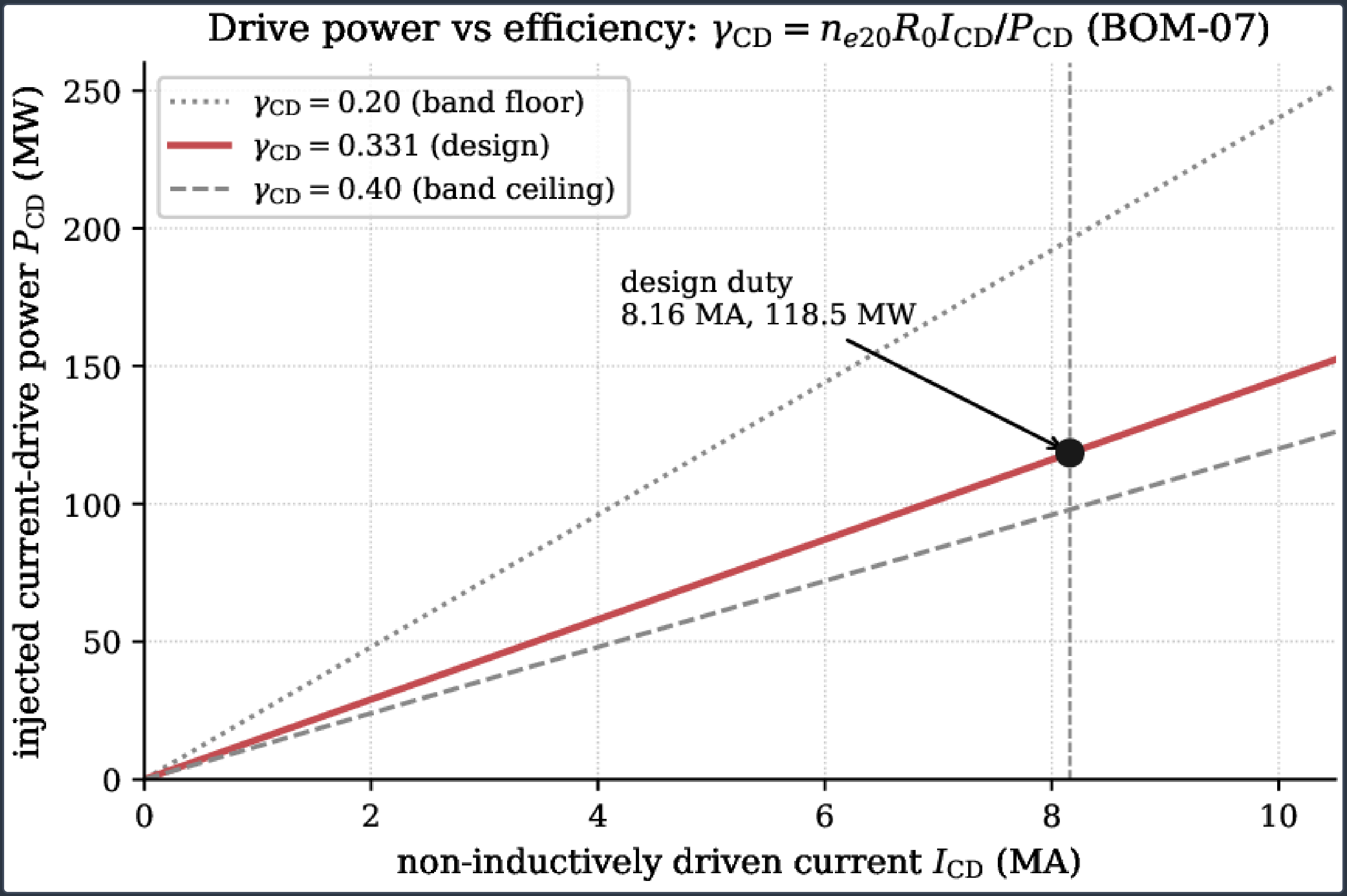

Injected current-drive power versus driven current at fixed normalized efficiency $\gamma_{CD} = n_{e20} R_0 I_{CD} / P_{CD}$ (eq. 10; BOM-07). The design duty ($8.16\,MA$, $118.5\,MW$) sits on the $\gamma_{CD} = 0.331$ contour; the 0.20–0.40 band brackets it. The inverse scaling of P_{CD} with γ_{CD} is why drive efficiency is the binding shadow price of equation (20).

DEPOSITION, FREQUENCY LANDSCAPE, AND THE PHYSICAL CONSTRAINTS

Figure 4 shows the representative off-axis deposition the negative-triangularity regime demands: the bootstrap seed peaks off-axis, NBCD deposits broadly, ECCD deposits in a narrow steerable band, and LHCD supports the outer radius. Figure 4 is the electron-cyclotron frequency landscape of equation (13): the $224\,\mathrm{Hertz} fundamental, the 180$ O-mode cutoff, and the underdense-core / overdense-edge boundary at $\omega_{pe}/\omega_{ce} = 0.80$ that mandates EBW coupling at the edge. Figure 5 shows the equatorial-port-area budget, saturated at 0.720 against the $0.719\,\mathrm{m}^2$ envelope and dominated 67% by NBI, together with the -0.4% streaming penalty on the local tritium-breeding ratio. Figure 5 shows the impurity-radiation budget of equation (17): the $0.19\,MW$ per ppm tungsten sensitivity that the impurity-transport controller holds. Figure 6 shows the admissible current window in the (q_{95}, I_p) plane — $I_p \in [8.779, 9.656]\,\mathrm{MA}$ over $q_{95} \in [2.7, 3.3]$, bounded above by the centrepost damage ceiling of 18.85 dpa fpy^{-1} (KX-L1-A21) — within which the H&CD duty is defined; this is the operating envelope of the lifetime-constrained window synthesis [doi:10.5281/zenodo.22645799; https://www.kronosfusionenergy.com/publications/admissible-operating-window-synthesis.html]companionOW.

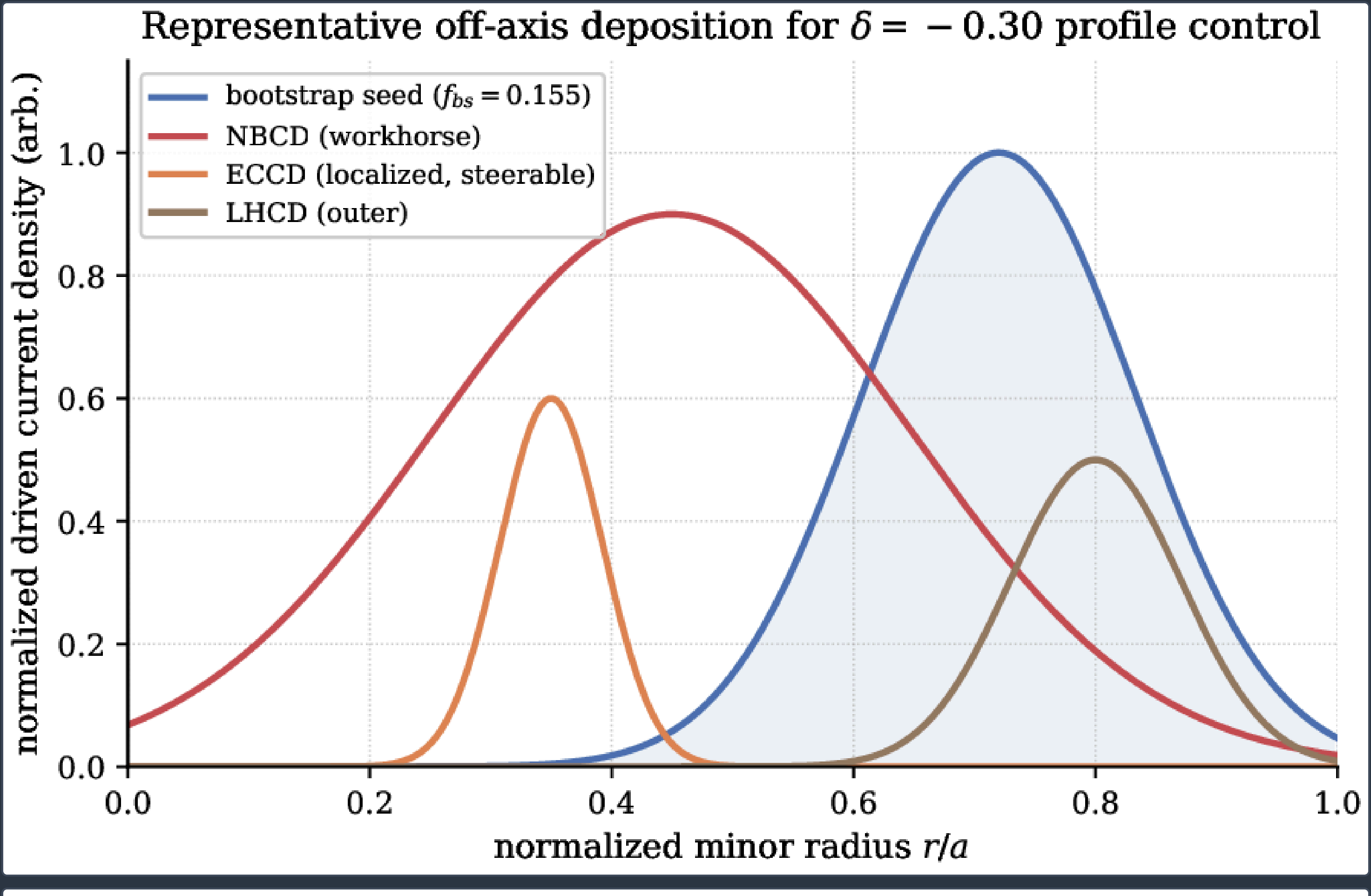

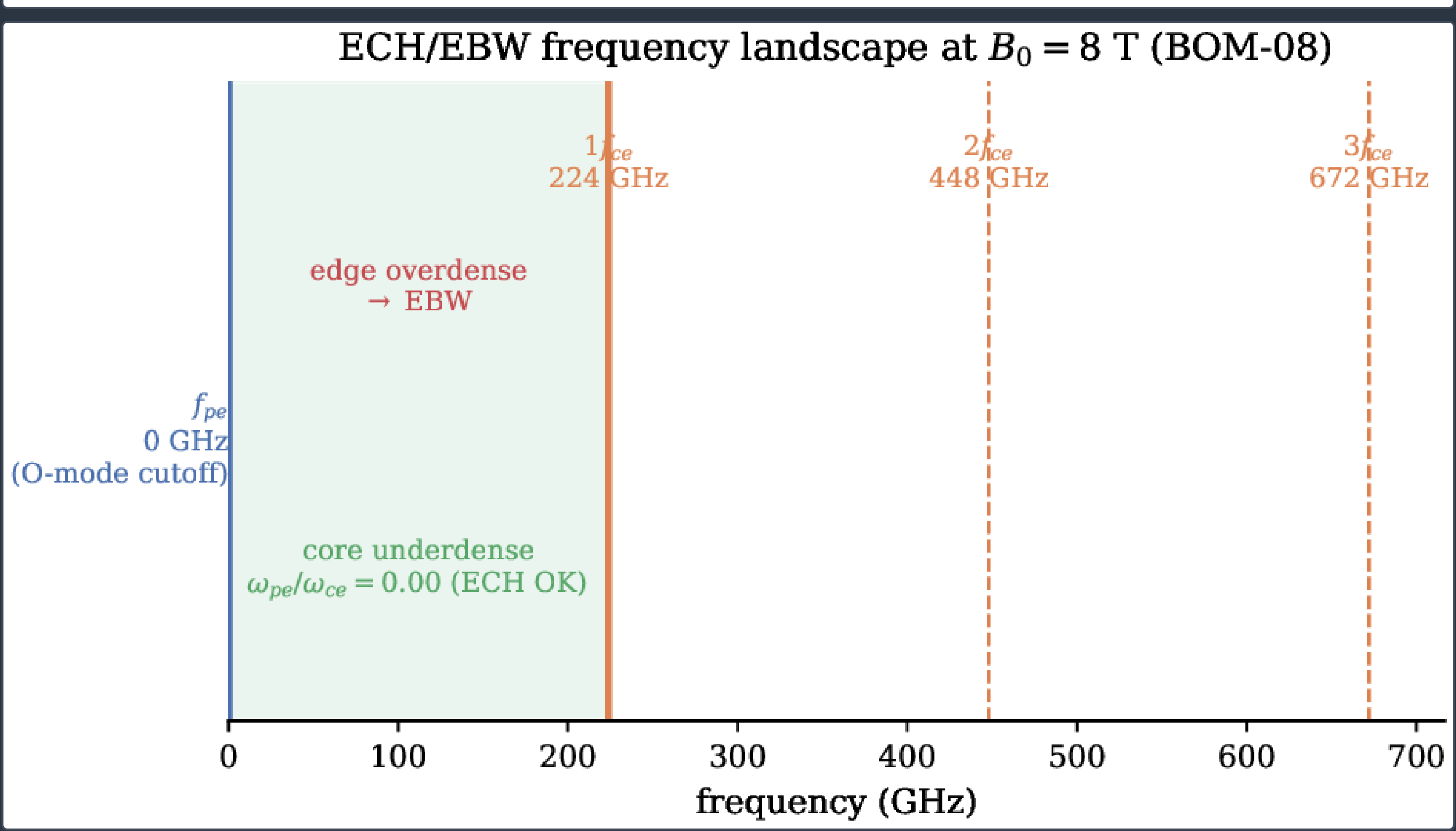

Representative off-axis deposition profiles for $\delta = -0.30$ profile control (shape derived from the design point; see §3). Bootstrap seed peaks off-axis; NBCD broad; ECCD narrow and steerable; LHCD outer.

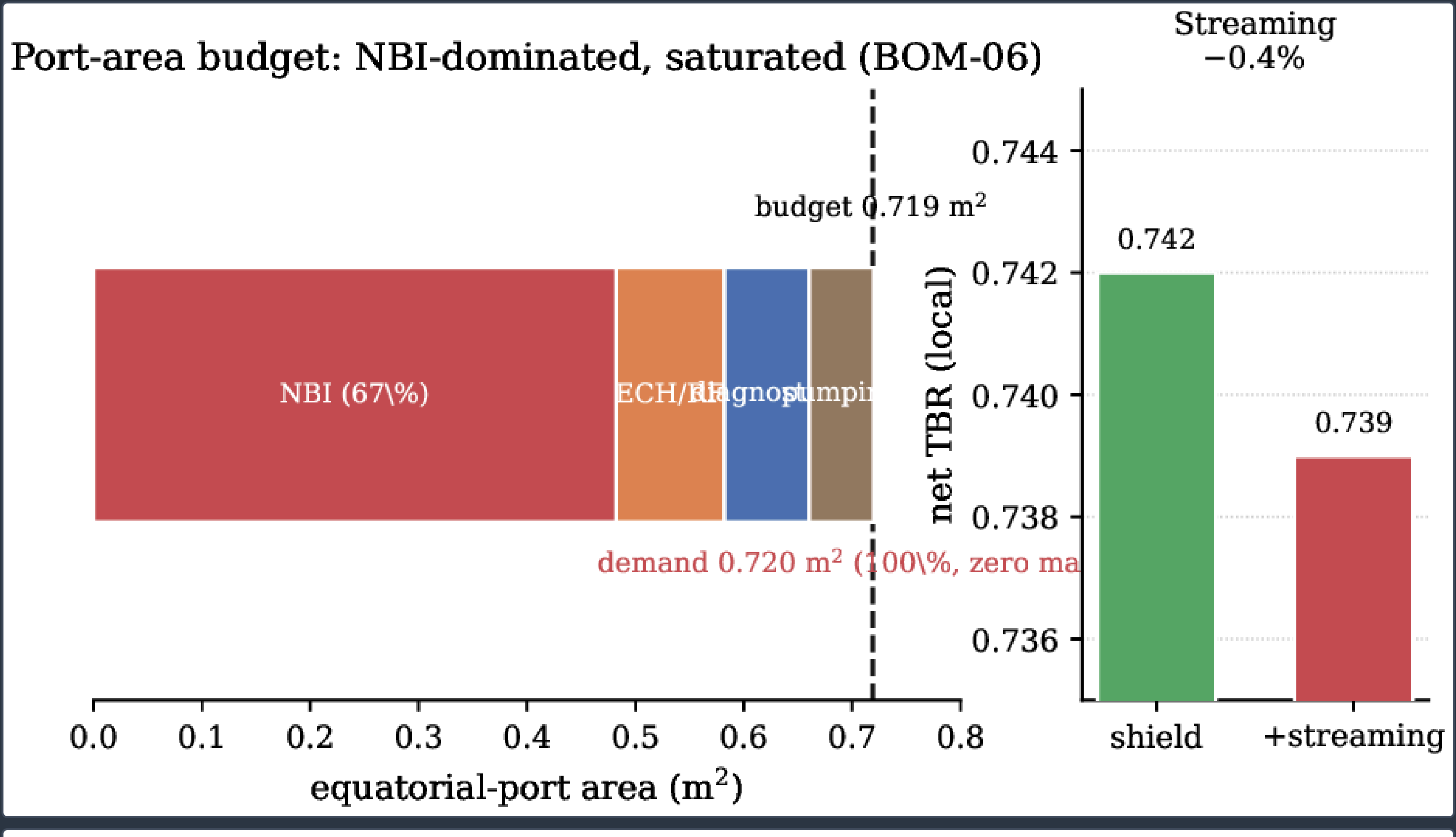

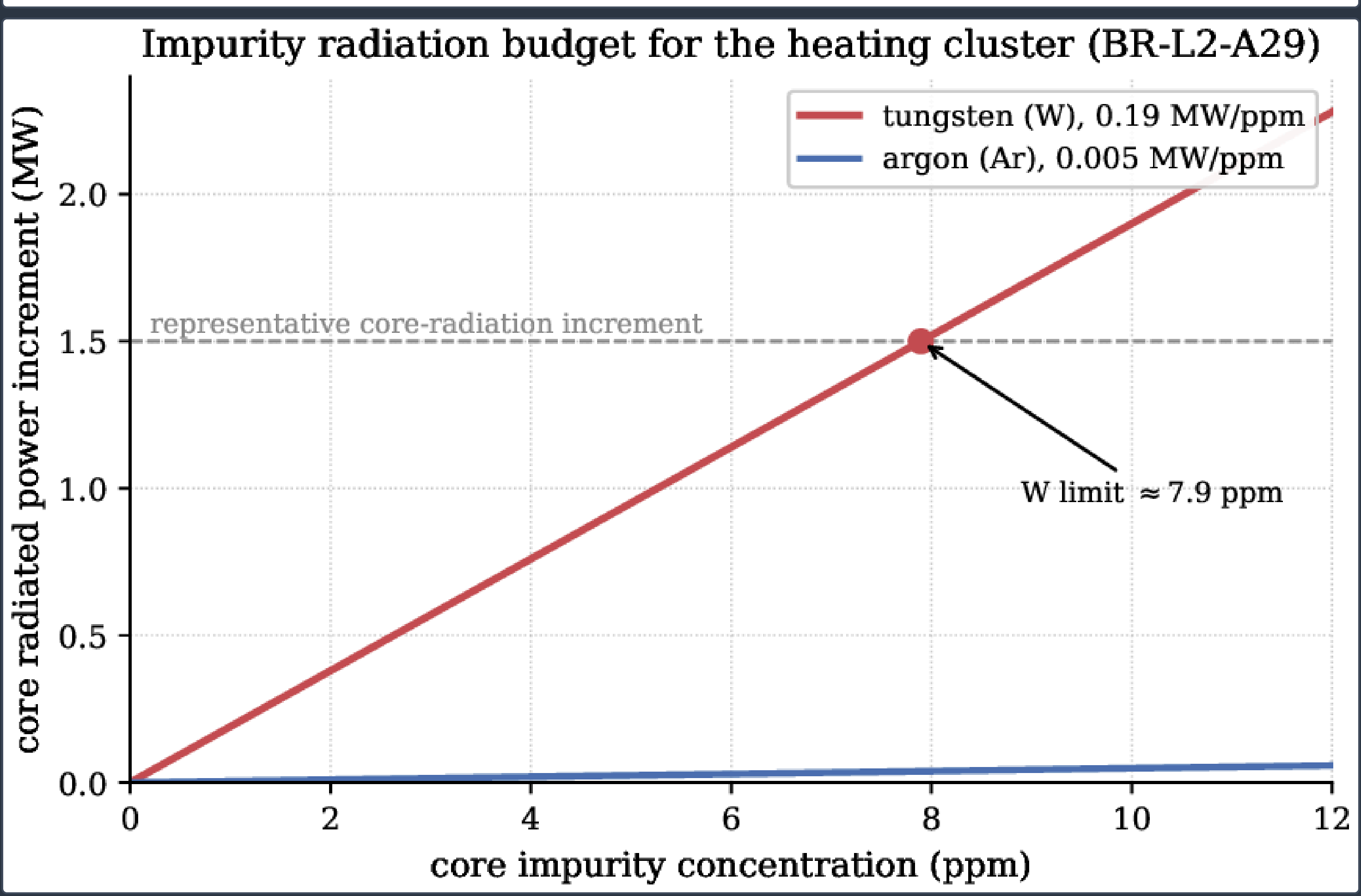

Equatorial-port-area budget (BOM-06): demand $0.720\,m^2$ saturates the $0.719\,m^2$ envelope, NBI-dominated (67%); the beam dog-leg costs −0.4% on the local tritium-breeding ratio (0.742 → 0.739).

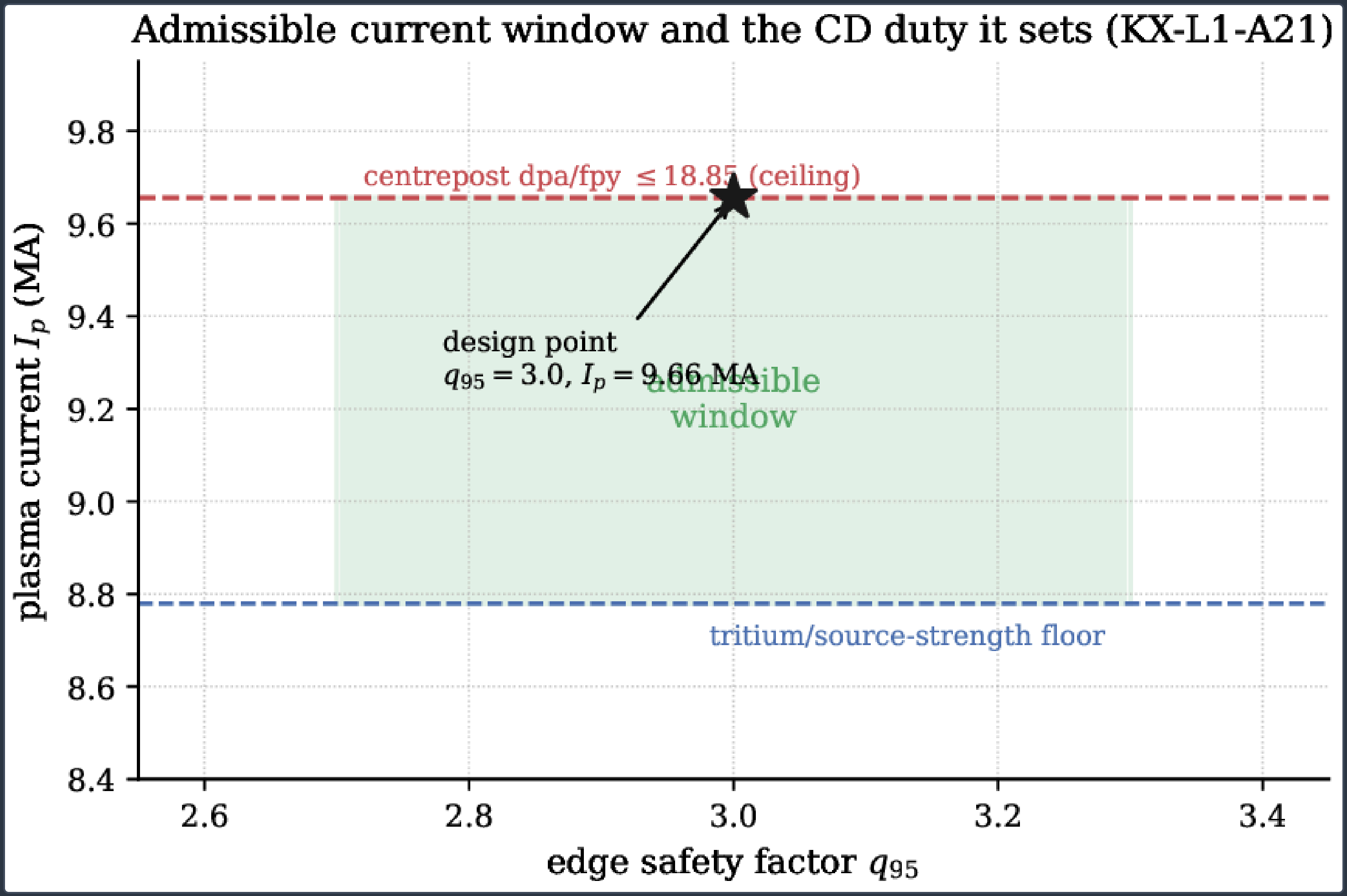

Admissible current window in the (q_{95}, I_p) plane (KX-L1-A21): $I_p \in [8.779, 9.656]$ MA over $q_{95} \in [2.7, 3.3]$, bounded above by the centrepost damage ceiling 18.85 dpa fpy^{-1}. The H&CD duty of §2 is defined at the design point (star).

ACCEPTANCE-CRITERIA STATUS

Table 4 collects the controller acceptance criteria of §7 with their targets and current status. The governing physics (bootstrap fraction, current-drive efficiency, deposition, frequency landscape, port and radiation budgets) is demonstrated at frozen-anchor fidelity; the controllers are pre-registered against the demonstrated pattern and are staged, not claimed as measured hardware.

CRITERION	TARGET / VALUE	STATUS (SERIAL)
bootstrap fraction f_{bs}	0.155 (NEO)	frozen (BR-L2-A6)
driven current I_{CD}	8.16 MA	frozen (BOM-07)
CD efficiency γ_{CD}	0.331 (band 0.20–0.40)	frozen (BOM-07)
ECH landscape ω_{pe}/ω_{ce}	0.80 at 224 $Hertz	frozen (BOM-08)
port-area budget	0.720 vs 0.719 m^2	frozen (BOM-06)
tungsten radiation tolerance	0.19 MW	frozen (BR-L2-A29)
power tracks set-point	±tolerance	staged (KFE-CF-SH-045)
mix meets target at least power	optimum of eq. (18)	staged (KFE-CF-BR-074)

table continued

drive efficiency improved	$\uparrow \gamma_{\mathrm{CD}}$	staged (KFE-CF-BR-073)
deposition on target	$\lVert j - j_{\mathrm{tgt}} \rVert \leq \delta_j$	staged (KFE-CF-BR-072)
shine-through within wall limit	$S \leq S_{\max}$	staged (KFE-CF-SH-113)
reflected power minimised	$\lvert\Gamma\rvert^2 \to \min$	staged (KFE-CF-SH-114)

REAL-TIME TIERING AND GRID INTERFACE

Table 5 gives the design allocation of the controllers to real-time tiers, with the fast protective loop (shine-through, impedance) never gated behind the slower optimiser tier. The plant's pulsed-load interface is a power-systems, not an economic, quantity: the NBI-dominated import of $\sim 520\,MW$ and the pulsed swing of $\sim 250\,MW$ require a point of common coupling of $\gtrsim 9.3$ GVA or a STATCOM-plus-flywheel buffer to hold the voltage dip below 3% (BOM-09), which bounds the actuator ramp rates the power controller may command.

LOOP	CONTROLLERS	LATENCY CLASS
fast (protective)	shine-through monitor, impedance matcher	microsecond–sub-ms (RT/FPGA)
medium (execute)	power controller, ECH mirror-steering	milliseconds (twin)
slow (optimise)	heating-mix, CD-efficiency, impurity, bootstrap est.	10^1–10^2 ms (GPU/twin)

Design real-time tiering of the H&CD controllers (BOM/KFE-CF workplan). Allocations, not measurements.

§ 9

Discussion

THE CURRENT-DRIVE SOLUTION AGAINST THE PUBLISHED LITERATURE

The design point should be read against the established H&CD literature. The normalized efficiency $\gamma_{\mathrm{CD}} = 0.331$ (BOM-07) falls squarely inside the $0.2–0.4$ range reported for negative-ion NBCD and for the ITER steady-state scenarios of the ITER Physics Basis [20,19], so the drive solution does not rest on an optimistic efficiency, and the $1\,MeV$ negative-ion beams are exactly the regime for which positive-ion neutralisation fails. On the wave side, the underdense core ($\omega_{pe}/\omega_{ce} = 0.80$) keeps O-/X-mode ECCD accessible via the Fisch–Boozer and Ohkawa mechanisms benchmarked by Prater and co-workers [7,12,13], while the overdense edge places the device in the electron-Bernstein-wave regime [18] — a known, if demanding, coupling route, not a novel physics claim; LHCD is retained for the outer radius within the modest accessibility floor of equation (16) [14].

WHY EFFICIENCY, NOT POWER, IS THE DESIGN DRIVER

The distinctive quantitative feature of a breeder is the gap between the gain-basis heating power ($27.6\,MW$) and the current-drive power ($118.5\,MW$). In a conventional net-power tokamak the two are comparable and heating dominates the discussion; here the current-drive burden is more than four times larger, and the KKT analysis of §4 shows why this reorients the whole architecture. When the current constraint (18) binds, its shadow price scales as $1/\gamma_{\mathrm{CD}}$ (equation 20), so the marginal value of a fractional gain in drive efficiency is set by the entire $118.5\,MW$ drive budget, not by the smaller heating budget. This is the formal justification for placing the current-drive-efficiency optimiser (KFE-CF-BR-073) at the top of the controller stack and for the functional redundancy of the complement, which exists precisely so the optimiser has degrees of freedom to exploit. It is also why the negative-triangularity, ELM-free edge is an operational asset for this system: it removes the transient edge loads that would otherwise force conservative, low-efficiency operation (BR-CX-08).

RELATION TO LEARNED AND INTEGRATED CONTROL

The architecture is complementary to learned control. Degrave and co-workers demonstrated a deep reinforcement-learning policy commanding coil voltages on TCV directly from magnetics, including negative-triangularity shapes [29]; that is a learned policy acting on the present measurement, whereas the H&CD controllers specified here are model-based and physics-grounded, each carrying an explicit acceptance test and admitted to authority through a maturity gate. The two compose: a learned policy can act within the envelope that table 4 defines, inheriting the physics constraints of §3. Relative to a purely learned controller, the contribution here is the first-principles derivation of the duty, the transparent optimisation whose multipliers identify the binding quantity, and the reproducible GPU code stack behind every number.

§ 10

Limitations

One honest gate bounds the claims. The governing physics and the design-point figures — $f_{bs} = 0.155$, $I_{CD} = 8.16\,MA$, $\gamma_{CD} = 0.331$, the frequency landscape, and the port and radiation budgets — are reproduced, frozen register anchors; the six controllers are specified and validated against high-fidelity plant-twin simulation but not yet on hardware. Hardware-in-the-loop validation on the actuator benches — the negative-ion beam source at full energy, the **224** Hertz $gyrotron, and the ICRF antenna under time-varying loading --- is the confirming step and the one staged item, entered on the same maturity gate that governs every controller in the architecture (figure$??? $). The$ 224 gyrotron in particular is at the frontier of tube development and is flagged as a technology-readiness item (BOM-08).

§ 11

Conclusion

The heating and current-drive system for the Hyperion breeder is derived from its duty rather than assembled from a hardware catalogue. The design point fixes that duty completely: sustain $9.66\,MA$ non-inductively with a bootstrap seed of only $f_{\text{bs}} = 0.155$, which forces $8.16\,MA$ of externally driven current and, at $\gamma_{\text{CD}} = 0.331$, an injected drive power of $118.5\,MW$ — more than four times the $27.6\,MW$ gain-basis heating power, marking the breeder as a current-drive-dominated, subcritical neutron source. We wrote the four sources as explicit governing equations, posed the allocation of power as a constrained nonlinear program whose KKT multipliers make drive efficiency the binding shadow price, gave the coupled fixed-point numerical formulation and the GPU-accelerated code stack that produced every number, and specified a four-technology complement — NBI, ECH/ECCD, ICRF, LHCD — operated by six real-time controllers, each with an explicit acceptance test and a maturity-gated path to authority. Benchmarked against the published NBCD/ECCD/LHCD literature the design point is unremarkable in its physics and defensible in its efficiency, which is the intended result: an H&CD architecture defined by the physics it must serve and staged cleanly toward hardware.

Acknowledgments tocsectionAcknowledgments Part of the Kronos Fusion Energy 2026 design series. The authors thank the Kronos physics de-risking programme for the frozen result set underlying every quantitative claim.

Reproducibility. The design-point anchors ($I_p = 9.66\,MA$, $P_{\text{fus}} = 85.04\,MW$, $Q = 3.076$; BR-L1-A1/A7), the neoclassical bootstrap fraction ($f_{\text{bs}} = 0.155$; BR-L2-A6/A16), the current-drive solution ($I_{\text{CD}} = 8.16\,MA$, $\gamma_{\text{CD}} = 0.331$, $P_{\text{CD}} = 118.5\,MW$; BOM-07), the ECH frequency landscape (BOM-08), the port-area budget (BOM-06), and the impurity-radiation tolerance (BR-L2-A29) are frozen results in the Kronos Physics De-Risking Register (doi:10.5281/zenodo.22133057). Each figure is regenerable from the archived numbers by the deposited figure-generation script (`make_hcd_figs_2103.py`). This paper is archived at its DOI doi:10.5281/zenodo.22645872 and its official page https://www.kronosfusionenergy.com/publications/heating-and-current-drive-actuator-systems-for-a-compac.html; the register is archived at doi:10.5281/zenodo.22133057.

Data availability tocsectionData availability The current and power budgets, the current-drive-efficiency contours, the ECH frequency landscape, the port-area and impurity-radiation budgets, and the admissible-window map used for figures 2–6 are archived with the deposit at doi:10.5281/zenodo.22645872, which references the Kronos 2026 series register (doi:10.5281/zenodo.22133057). All quantitative values trace to the register by the serial identifiers cited inline. Any economic analysis is reported separately and is not part of the public deposit.

Competing interests tocsectionCompeting interests Provisional patent applications relating to aspects of this work have been filed.

tocsectionReferences

APPARATUS

Portfolio, People & Record

The intellectual-property estate, the people who built it, the limitations that gate it, and the sources it rests on.

1	4	40	27
GRANTED PATENT	2026 PROVISIONALS	TEAM MEMBERS	2022 PROVISIONALS

INTELLECTUAL PROPERTY

The patent portfolio

The estate spans a granted high-field magnet patent, pending utility and 2026 provisional filings that map to the two products, a digital-twin control provisional, a registered trademark application, and the original 2022 provisional family. Every patentable disclosure in the five-paper arXiv drop was protected **before** publication: the breeder and burner provisionals were filed 1–2 August, and a publication-gap omnibus filing the evening before the drop swept up the DEC, plasma-control, and REBCO-winding matter of the three otherwise-unprotected papers. Patent numbers and application serials are matters of public record; claim scope is summarised, not reproduced.

GRANTED & PENDING UTILITY

US 12,009,112	High-field tilted graded-REBCO magnet architecture (KRONO-002A) · *app. 17/878,550*	GRANTED
US 17/878,507	Core device / method (KRONO-001A) · *utility*	PENDING

2026 PROVISIONAL FILINGS — MAPPED TO THE PRODUCTS

64/124,209	Hyperion — spherical-tokamak tritium / helium-3 foundry · *breeder · filed Aug 2026*	FILED
64/124,220	Aegis / MetroVolt — synchrotron-cutoff, fuel-selection & plug-winding · *generator · filed Aug 2026*	FILED
64/115,167	KRONOS-CTRL digital-twin plant control · *provisional · filed Jul 2026*	FILED
64/005,440	Integrated spherical-tokamak fusion architecture · *early integrated-architecture filing · filed Mar 2026*	FILED
64/105,530	Negative-triangularity spherical-tokamak architecture · *foundational ST filing · filed Jul 2026*	FILED
64/128,097	Publication-gap omnibus — quasineutral two-species expander DEC · provenance-gated / latency-split plasma control · as-built high-field winding & conductor architecture · *filed 7 Aug 2026, the evening before the arXiv drop*	FILED

TRADEMARK & ORIGIN

FTK-98801894	Kronos Fusion Energy — trademark application	FILED
KR-2022-*	Original provisional family (KR-2022-00001 … 00027) · *27 filings, 2022*	PRIORITY

The narrow, defensible magnet novelty — the specific conductor and the digital-twin winding optimisation, not high-field REBCO as a category — is the commercial core that can earn ahead of any $Q > 1$ milestone, with markets in fusion magnet supply, MRI/NMR, accelerators, and proton therapy. The claim is scoped honestly: the high field is a *system field* result, not a stand-alone-coil record; the small-bore plug coil is structurally infeasible as a bare winding but resolved by a stress-managed structural shield (feasible-pending-FEA); and the winding-tape experiment returned a *null result*. The value is the method, not a field record.

THE TEAM

Founding partners, board, advisors & auditors

Kronos is built by a bench of advanced-fuel-fusion, high-field-magnet, direct-conversion, and materials specialists, with a board and operations team drawn from defense, national laboratories, and industry. Dates are shown as ranges; where a tenure has ended or is term-ending, the range says so.

FOUNDING PARTNERS — SCIENCE

Dr. Gerald Kulcinski
Co-Founder · Helium-3 & Advanced-Fuel Fusion
UW–Madison · 2023–Present

Dr. Carl Weggel
Chief Scientist / S.M.A.R.T. Design
MIT Alcator Program · 2022–Present

Dr. Robert J. Weggel
Magnetic Field Design
MIT Magnet Lab · 2022–Present

BOARD

Priyanca Ford
Founder & CEO · Executive Board
2022–Present

Bandel Carano
Finance / Strategy
Oak Investment Partners / Stanford · 2025–2026

Patrick Schweiger
Fusion Device Engineering
Oklo / CFS / TerraPower · 2025–Present

SCIENTIFIC ADVISORS

Dr. Steven O. Dean
Fusion Policy & History
DOE / Fusion Power Associates · 2025–Present

Dr. Patrick H. Diamond
Plasma Turbulence & Transport
UC San Diego · 2025–Present

Dr. Jack J. Dongarra
HPC & Numerical Algorithms
Turing Award · 2025–Present

Dr. Nasr M. Ghoniem
Chief Material Scientist
UCLA · 2025–Present

Dr. Siegfried Glenzer
Plasma Physics & Laser Fusion
Stanford / SLAC · 2022–Present

Dr. David A. Hammer
Pulsed-Power Fusion
Cornell · 2025–Present

Dr. Donald A. Spong
Plasma Theory & Confinement
ORNL · 2025–Present

Dr. Curtis Smith
Risk Assessment & Nuclear PRA
MIT / Idaho National Lab · 2025–Present

RADM (Ret.) David Goggins
Naval Engineering & Power-Plant Design
U.S. Navy · 2023–2026

Dr. Konstantin Batygin
Mathematician
Caltech · 2022–2025

Dr. Ruben Fair
Magnet Design / ITER Liaison
PPPL / Jefferson Lab · 2022–2025

Dr. Paul S. Weiss
Materials & Nanotechnology
UCLA · 2022–2025

SCIENTIFIC AUDITORS

Dr. Wilfred A. Cooper
Plasma Equilibrium Theory
EPFL / Swiss Plasma Center · 2025–Present

Dr. Ahmed Hassanein
Plasma–Material Interactions
Purdue / Argonne · 2025–Present

Dr. Patrick E. Hopkins
Extreme Thermal Materials
U. of Virginia · 2025–Present

Dr. Peter Hosemann
Materials Joining & Structural Integrity
UC Berkeley · 2025–Present

Dr. Travis W. Knight
Advanced Nuclear Fuels & Systems
U. of South Carolina · 2025–Present

Dr. Philippe Lebrun
Cryogenics & Magnet Cooling
CERN · 2025–Present

Dr. Nitendra Singh
Nuclear Safety & Fuel Cycle
ITER · 2025–Present

Dr. Guido Van Oost
Magnetic Confinement & Fusion Systems
Ghent University · 2025–Present

Dr. Gary S. Was
Radiation Materials & Structural Integrity
U. of Michigan · 2025–Present

Dr. Ray Sedwick
Direct Energy Conversion
U. of Maryland · 2025

OPERATIONS

Michael Laughlin
Chief Operating Officer
2022–Present

Martin Owens
Chief Strategy Officer
LANL / GE Hitachi · 2022–Present

MG (Ret.) Paul Pardew
Chief Contracting Officer
Army Contracting Command · 2022–Present

David Beck
Fusion Commercialization
U.S. Space Force · 2024–Present

Sushma Bhatia
Environmental & Legislative
Google · 2022–Present

Michael De Frenza
Technology Licensing
2023–Present

MG (Ret.) Robin L. Fontes
Cybersecurity & Defense
Army Cyber Command · 2022–Present

Vijay Gehani
Supply Chain & Components
INOX India · 2024–Present

Jon Michel Greenwood
IT & AI Infrastructure
Live Nation · 2023–Present

Brian C. O'Neill
National Security
CIA / ODNI · 2022–Present

Gen. (Ret.) Gustave F. Perna
DoD Liaison
Operation Warp Speed · 2022–2023

Andrea Romero
Marketing Lead
2022–Present

Legal counsel is retained; those roles are held on the internal roster and are not listed here.

SOURCES

References

1 J E Menard *et al*, Fusion nuclear science facilities and pilot plants based on the spherical tokamak, *Nucl. Fusion* **56** 106023 (2016). doi:10.1088/0029-5515/56/10/106023

2 B N Sorbom *et al*, ARC: a compact, high-field, fusion nuclear science facility and demonstration power plant with demountable magnets, *Fusion Eng. Des.* **100** 378 (2015). doi:10.1016/j.fusengdes.2015.07.008

3 M Ono *et al*, Exploration of spherical torus physics in the NSTX device, *Nucl. Fusion* **40** 557 (2000).

4 M E Austin *et al*, Achievement of reactor-relevant performance in negative triangularity shape in the DIII-D tokamak, *Phys. Rev. Lett.* **122** 115001 (2019). doi:10.1103/PhysRevLett.122.115001

5 A Marinoni, O Sauter and S Coda, A brief history of negative triangularity tokamak plasmas, *Rev. Mod. Plasma Phys.* **5** 6 (2021). doi:10.1007/s41614-021-00054-0

6 N J Fisch, Theory of current drive in plasmas, *Rev. Mod. Phys.* **59** 175 (1987).

7 N J Fisch and A H Boozer, Creating an asymmetric plasma resistivity with waves, *Phys. Rev. Lett.* **45** 720 (1980).

8 T Ohkawa, New methods of driving plasma current in fusion devices, *Nucl. Fusion* **10** 185 (1970).

9 D F H Start, J G Cordey and E M Jones, The effect of trapped electrons on beam driven currents in toroidal plasmas, *Plasma Phys.* **22** 303 (1980).

10 O Sauter, C Angioni and Y R Lin-Liu, Neoclassical conductivity and bootstrap current formulas for general axisymmetric equilibria and arbitrary collisionality regime, *Phys. Plasmas* **6** 2834 (1999).

11 E A Belli and J Candy, Kinetic calculation of neoclassical transport including self-consistent electron and impurity dynamics (NEO), *Plasma Phys. Control. Fusion* **50** 095010 (2008).

12 R Prater, Heating and current drive by electron cyclotron waves, *Phys. Plasmas* **11** 2349 (2004).

13 R Prater *et al*, Benchmarking of codes for electron cyclotron heating and electron cyclotron current drive under ITER conditions, *Nucl. Fusion* **48** 035006 (2008).

14 P T Bonoli, Review of recent experimental and modeling progress in the lower hybrid range of frequencies at ITER-relevant parameters, *Phys. Plasmas* **21** 061508 (2014).

15 T H Stix, Fast-wave heating of a two-component plasma, *Nucl. Fusion* **15** 737 (1975).

16 E F Jaeger *et al*, Self-consistent full-wave and Fokker–Planck calculations for ion cyclotron heating in non-Maxwellian plasmas, *Phys. Plasmas* **13** 056101 (2006).

17 M Brambilla, Numerical simulation of ion cyclotron waves in tokamak plasmas, *Plasma Phys. Control. Fusion* **41** 1 (1999).

18 H P Laqua, Electron Bernstein wave heating and diagnostic, *Plasma Phys. Control. Fusion* **49** R1 (2007).

19 ITER Physics Expert Group on Energetic Particles, Heating and Current Drive, Chapter 6: Plasma auxiliary heating and current drive, *Nucl. Fusion* **39** 2495 (1999).

20 C Gormezano *et al*, Chapter 6: Steady state operation, Progress in the ITER Physics Basis, *Nucl. Fusion* **47** S285 (2007).

21 A Pankin, D McCune, R Andre, G Bateman and A Kritz, The tokamak Monte Carlo fast ion module NUBEAM in the National Transport Code Collaboration library, *Comput. Phys. Commun.* **159** 157 (2004).

22 R W Harvey and M G McCoy, The CQL3D Fokker–Planck code, *Proc. IAEA Tech. Comm. Meeting on Advances in Simulation and Modeling of Thermonuclear Plasmas* (Montreal) p 489 (1992).

23 A P Smirnov and R W Harvey, The GENRAY ray tracing code, CompX Report CompX-2000-01 (2001).

24 G M Staebler, J E Kinsey and R E Waltz, A theory-based transport model with comprehensive physics, *Phys. Plasmas* **14** 055909 (2007).

25 J Candy, E A Belli and R V Bravenec, A high-accuracy Eulerian gyrokinetic solver for collisional plasmas, *J. Comput. Phys.* **324** 73 (2016). doi:10.1016/j.jcp.2016.07.039

26 N C Amorisco *et al*, FreeGSNKE: a Python-based dynamic free-boundary toroidal plasma equilibrium solver, *Phys. Plasmas* **31** 042517 (2024).

27 L L Lao, H St John, R D Stambaugh, A G Kellman and W Pfeiffer, Reconstruction of current profile parameters and plasma shapes in tokamaks, *Nucl. Fusion* **25** 1611 (1985). doi:10.1088/0029-5515/25/11/007

28 F Felici *et al*, Real-time physics-model-based simulation of the current density profile in tokamak plasmas, *Nucl. Fusion* **51** 083052 (2011). doi:10.1088/0029-5515/51/8/083052

29 J Degrave *et al*, Magnetic control of tokamak plasmas through deep reinforcement learning, *Nature* **602** 414 (2022). doi:10.1038/s41586-021-04301-9

30 P I Ford, Negative-triangularity turbulence suppression in a compact spherical-tokamak breeder, Kronos Fusion Energy 2026 series. doi:10.5281/zenodo.22645722. https://www.kronosfusionenergy.com/publications/negative-triangularity-confinement.html

31 P I Ford, Bootstrap-aligned steady-state current sustainment without a central solenoid: NBCD, ECCD and LHCD for a compact spherical-tokamak breeder, Kronos Fusion Energy 2026 series. doi:10.5281/zenodo.22645758. https://www.kronosfusionenergy.com/publications/current-drive-and-bootstrap.html

32 P I Ford, From breakdown to flat-top: solenoid-free startup and disruption-free ramp access for a negative-triangularity spherical-tokamak breeder, Kronos Fusion Energy 2026 series. doi:10.5281/zenodo.22645760. https://www.kronosfusionenergy.com/publications/solenoid-free-startup.html

33 P I Ford, A real-time control suite for a compact negative-triangularity spherical-tokamak breeder, Kronos Fusion Energy 2026 series. doi:10.5281/zenodo.22645809. https://www.kronosfusionenergy.com/publications/a-real-time-control-suite-for-a-compact-negative-triang.html

34 P I Ford, Four coupled digital twins for a compact spherical-tokamak breeder, Kronos Fusion Energy 2026 series. doi:10.5281/zenodo.22645805. https://www.kronosfusionenergy.com/publications/four-coupled-digital-twins-for-a-compact-spherical-toka.html

35 P I Ford, Maturity-gated actuation authority: binding PCMM verification credibility to runtime control authority, Kronos Fusion Energy 2026 series. doi:10.5281/zenodo.22645795. https://www.kronosfusionenergy.com/publications/maturity-gated-actuation-authority.html

36 P I Ford and G L Kulcinski, Lifetime-constrained operating-window synthesis for a compact spherical-tokamak breeder, Kronos Fusion Energy 2026 series. doi:10.5281/zenodo.22645799. https://www.kronosfusionenergy.com/publications/admissible-operating-window-synthesis.html

37 P I Ford, Verification-first fusion modeling: frozen anchors, independent-library gate reproduction and a byte-for-byte computational-provenance catalog, Kronos Fusion Energy 2026 series. doi:10.5281/zenodo.22645710. https://www.kronosfusionenergy.com/publications/verification-and-validation-47-code-provenance.html

38 P I Ford, The code-by-code verification backbone, Kronos Fusion Energy 2026 series. doi:10.5281/zenodo.22645866. https://www.kronosfusionenergy.com/publications/the-code-by-code-verification-backbone-role-version-and.html

39 P I Ford, *Kronos Physics De-Risking Register*, Kronos Fusion Energy 2026 series. doi:10.5281/zenodo.22133057

COLOPHON

How this document was made

The Kronos Fleet — Combined Editorial, 2026 is set in **Fraunces** (display), **Gelasio** (text), and **IBM Plex Mono** (data & equations), carried forward from the Kronos editorial design system.

The figures are rendered at 300 dpi from the deposited generator scripts; the document is composed as a single self-contained file with embedded fonts and imagery, paginated to US Letter, and rendered to PDF through a headless Chromium engine in matched light and dark editions.

Every headline quantity carries an evidence class; withdrawn and restated values are marked as such. Nothing herein is frozen beyond the founder-approved Tier-A set.

Explore it live — turn the interactive 3-D model, run the deposited solvers in the physics validator, and watch the companion film series.

LEGAL NOTICE

Notice, status, and distribution

Conceptual design & simulation study. This document reports a conceptual design and simulation study. It is not a construction commitment, a safety-analysis report, a regulatory filing, or an offer of securities. Forward-looking statements — schedules, costs, market sizes, and performance — are estimates subject to the limitations set out in the Simulations part and may change.

Numbers and their classes. Quantities are reported with evidence classes and case labels; modelled, assumed, and requirement-class values are identified as such and are not to be quoted without their labels.

Public edition. This edition carries the physics and design only; all financial, funding, and defense-commercial content has been removed for public distribution. The scientific text corresponds to the arXiv and journal submissions.

THE 2026 KRONOS SERIES

One programme, many papers

This editorial is one paper in the Kronos 2026 series — a real fusion company's complete, reproducible physics record for a spherical-tokamak breeder and its low-neutron D–^{3}He tandem-mirror burners. Every headline number is a frozen anchor in the Physics De-Risking Register.

Explore the whole programme: the De-Risking Register, the interactive 3-D model, and the physics validator.

KRONOS FUSION ENERGY

Heating and Current-Drive Actuator Systems for a Compact Spherical-Tokamak Breeder: An NBI/ECH/ICRF/LHCD Mix Optimized for Solenoid-Free Sustainment

A real fusion company building real machines. Explore the science, live.

Zenodo · doi:10.5281/zenodo.22645872

Read on kronosfusionenergy.com

The Physics De-Risking Register